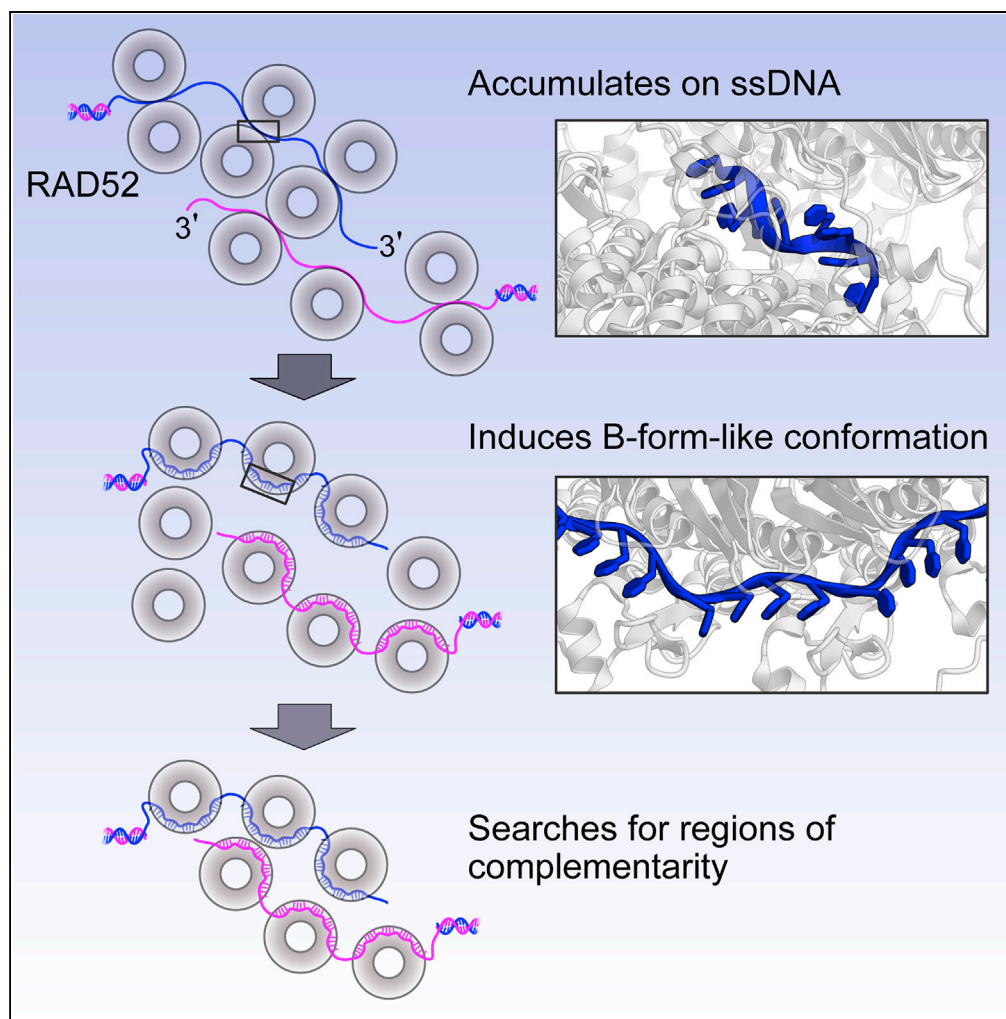**Article**

Structural Basis of Homology-Directed DNA Repair Mediated by RAD52

Mika Saotome, Kengo Saito, Takeshi Yasuda, ..., Yoshifumi Nishimura, Hitoshi Kurumizaka, Wataru Kagawa

kurumizaka@waseda.jp (H.K.)
wataru.kagawa@meisei-u.ac.jp (W.K.)

HIGHLIGHTS

The outer and inner DNA binding sites of RAD52 have different binding modes for ssDNA

The outer site has high affinity for ssDNA and promotes RAD52 accumulation on ssDNA

The inner site induces a B-form-like ssDNA conformation suitable for base pairing

The two sites cooperatively bind to ssDNA to promote DNA annealing

Article

Structural Basis of Homology-Directed DNA Repair Mediated by RAD52

Mika Saotome,[1,5] Kengo Saito,[2,5] Takeshi Yasuda,[3] Hideaki Ohtomo,[4] Shusei Sugiyama,[2] Yoshifumi Nishimura,[4] Hitoshi Kurumizaka,[2,*] and Wataru Kagawa[1,6,*]

SUMMARY

RAD52 mediates homologous recombination by annealing cDNA strands. However, the detailed mechanism of DNA annealing promoted by RAD52 has remained elusive. Here we report two crystal structures of human RAD52 single-stranded DNA (ssDNA) complexes that probably represent key reaction intermediates of RAD52-mediated DNA annealing. The first structure revealed a "wrapped" conformation of ssDNA around the homo-oligomeric RAD52 ring, in which the edges of the bases involved in base pairing are exposed to the solvent. The ssDNA conformation is close to B-form and appears capable of engaging in Watson-Crick base pairing with the cDNA strand. The second structure revealed a "trapped" conformation of ssDNA between two RAD52 rings. This conformation is stabilized by a different RAD52 DNA binding site, which promotes the accumulation of multiple RAD52 rings on ssDNA and the aggregation of ssDNA. These structures provide a structural framework for understanding the mechanism of RAD52-mediated DNA annealing.

INTRODUCTION

DNA double-strand breaks (DSBs) are formed by reactive oxygen species and ionizing radiation, as well as by replication over single-strand nicks and inadvertent actions of nuclear enzymes (Lieber, 2010; Mehta and Haber, 2014). Homology-directed repair (HDR) is an important mechanism for repairing DSBs (Ceccaldi et al., 2016; Pâques and Haber, 1999). Properly functioning HDR is critical for genomic stability. In eukaryotes, the failure of HDR can lead to gross changes in the chromosome structure, including an abnormal number of chromosomes (aneuploidy) and the loss of heterozygosity. These chromosomal alterations can have serious consequences, such as tumorigenesis (Jackson and Bartek, 2009; Moynahan and Jasin, 2010). The importance of HDR is underscored by the high conservation, from yeast to humans, of the proteins that catalyze the reaction (San Filippo et al., 2008; Krogh and Symington, 2004).

Multiple reaction pathways have been proposed for HDR (Heyer et al., 2010). They include double-strand break repair (DSBR), synthesis-dependent strand annealing (SDSA), break-induced replication (BIR), single-strand annealing (SSA), and alternative end joining (alt-EJ). Most of them involve the formation of a D-loop structure, which is a duplex DNA containing an invading homologous single-stranded DNA (ssDNA). The RecA/Rad51 recombinase family plays a central role in catalyzing this reaction. The formation of base pairs at the proper location between the invading ssDNA and the double-stranded DNA (dsDNA) is critical for the accurate repair. Depending on the HDR pathway, DNA annealing between complementary ssDNA regions can also influence the outcome of HDR (Bhargava et al., 2016; Ivanov et al., 1996). DNA annealing may occur spontaneously, but several proteins, such as Rad52, RecO, UvsY, RecT, Redβ, and ICP8, catalyze the reaction (Morrical, 2015).

Rad52 plays a multi-faceted role in HDR, and functions in both Rad51-dependent and Rad51-independent pathways. In yeast, mutations in Rad52 result in a severe recombination-deficient phenotype, indicating the importance of Rad52 in HDR (Game and Mortimer, 1974). Yeast Rad52 is believed to play two roles in HDR: facilitating the replacement of RPA with Rad51 on ssDNA (Song and Sung, 2000; Sugiyama and Kowalczykowski, 2002) and annealing cDNA strands (Mortensen et al., 1996; Sugiyama et al., 1998). The former role is correlated with the polymerization of Rad51 on ssDNA before D-loop formation and DNA strand exchange (Sung, 1997; Shinohara and Ogawa, 1998; New et al., 1998). By contrast, the latter role is probably more widely utilized in various HDR pathways, including DSBR, SDSA, and SSA. In humans, it is not clear whether RAD52 functions as a mediator of RAD51 (San Filippo et al., 2008). However,

[1]Department of Chemistry, Graduate School of Science and Engineering, Meisei University, 2-1-1 Hodokubo, Hino-shi, Tokyo 191-8506, Japan

[2]Laboratory of Structural Biology, Graduate School of Advanced Science and Engineering, Waseda University, 2-2 Wakamatsu-cho, Shinjuku-ku, Tokyo 162-8480, Japan

[3]National Institute of Radiological Sciences (NIRS), National Institutes for Quantum and Radiation Sciences and Technology (QST), 4-9-1 Anagawa, Inage-ku, Chiba 263-8555, Japan

[4]Graduate School of Medical Life Science, Yokohama City University, 1-7-29 Suehiro-cho, Tsurumi-ku, Yokohama 230-0045, Japan

[5]These authors contributed equally

[6]Lead Contact

*Correspondence: kurumizaka@waseda.jp (H.K.), wataru.kagawa@meisei-u.ac.jp (W.K.)

https://doi.org/10.1016/j.isci. 2018.04.005

like its yeast counterpart, RAD52 promotes DNA annealing (Reddy et al., 1997), which indicates that DNA annealing is a more widely conserved function among Rad52 orthologs. Human RAD52 is also capable of catalyzing the formation of D-loops *in vitro* (Kagawa et al., 2001), which may be a relevant activity in certain RAD51-independent pathways. Recently, RAD52 was demonstrated to function in the repair of collapsed DNA replication forks, via RAD51-independent BIR (Sotiriou et al., 2016; Bhowmick et al., 2016; Ciccia and Symington, 2016). Furthermore, RAD52 was implicated in promoting DNA repair in cancer cells, in which the RAD51-dependent repair pathway is defective (Feng et al., 2011; Lok et al., 2013). Although the precise role of RAD52 in these repair pathways remains obscure, understanding the molecular details of RAD52-mediated DNA annealing will be important for clarifying its functions in HDR (Hanamshet et al., 2016).

Yeast and human Rad52 form oligomeric rings (Shinohara et al., 1998; Stasiak et al., 2000; Ranatunga et al., 2001). Electron microscopic visualizations of Rad52 in the presence of ssDNA revealed that Rad52 forms aggregates on ssDNA and suggested that Rad52 rings engage in side-by-side interactions (Van Dyck et al., 1998). A positively charged groove running around the ring structure was identified from the crystal structures of the human RAD52 protein (Kagawa et al., 2002; Singleton et al., 2002). Mutagenesis studies suggested that this groove is a potential ssDNA binding site (Kagawa et al., 2002; Lloyd et al., 2005). Subsequent biochemical studies revealed that a region outside of the groove is a second DNA binding site (Kagawa et al., 2008). Mutations in this site impair the abilities of RAD52 to anneal complementary ssDNA strands, promote D-loop formation, and induce positive supercoils in DNA. Although these observations, along with DNA footprinting studies (Parsons et al., 2000; Singleton et al., 2002), are consistent with the view that the ssDNA wraps around the RAD52 ring, the precise path and structure of the ssDNA along the RAD52 surface is unclear. Furthermore, two DNA annealing mechanisms are conceivable: a *cis* mechanism, in which the complementary ssDNA strands bind and anneal on a single RAD52 ring (Kagawa et al., 2008), and a *trans* mechanism, in which annealing is promoted between two RAD52-ssDNA complexes (Rothenberg et al., 2008; Grimme et al., 2010). Further insights into the mechanism of the RAD52-mediated homology search require the structural details of the RAD52-ssDNA interactions.

In the present study, we determined two complex structures of human RAD52 and ssDNA, one in which the ssDNA is bound to the inner DNA binding site and the other wherein the ssDNA interacts with the outer DNA binding site of RAD52. The structures revealed clear differences in the ssDNA binding modes of the two DNA binding sites and suggest the means by which the inner and outer DNA binding sites participate in DNA annealing.

RESULTS

Structure of ssDNA Bound to the Inner DNA Binding Site of RAD52

The inner and outer DNA binding sites were previously identified from structural and mutagenesis studies of the N-terminal half of RAD52 (Kagawa et al., 2002, 2008). To understand the roles of these two DNA binding sites in RAD52-mediated DNA annealing, we first crystallized a 40-nucleotide ssDNA bound to the inner DNA binding site of the RAD52 homo-oligomeric ring and determined the structure of the complex by X-ray crystallography (Table 1). For crystallization, we used a truncated construct of the human RAD52 protein (referred to as RAD52 hereafter), lacking the C-terminal half (amino acid residues 213–418). The C-terminal half is structurally unstable, as revealed from previous limited proteolysis experiments (Kagawa et al., 2001), and prevented the full-length RAD52 from crystallizing. Importantly, multiple studies have shown that the full-length and C-terminally truncated RAD52 proteins display highly similar DNA binding properties (Parsons et al., 2000; Singleton et al., 2002; Kagawa et al., 2001, 2002; Lloyd et al., 2005). We incorporated two alanine substitutions distant from the inner DNA binding site (RAD52[1−212] K102A/K133A), which were essential for obtaining crystals that yielded interpretable electron density maps of the ssDNA (see Transparent Methods for details).

As predicted in previous studies, the ssDNA was accommodated inside the groove (Figure 1A). The electron density for the entire length of the ssDNA was clearly observed (Figure S1). The 40 nucleotides of ssDNA spanned across 10 subunits of the RAD52 ring (Figure 1B), and thus each subunit accommodated four nucleotides of the ssDNA. The phosphate backbone of the ssDNA was near the bottom of the groove, and the bases faced outward toward the solvent (Figures 1C–1E). This DNA binding mode is consistent with the fact that the deepest part of the groove is highly positively charged and appears to be suited for

	RAD52-ssDNA (Outer DNA Binding Site) (PDB: 5XS0)	RAD52-ssDNA (Inner DNA Binding Site) (PDB: 5XRZ)
Data Collection		
Space group	$P2_1$	$P1$
Cell dimensions		
a, b, c (Å)	100.22, 164.41, 166.09	67.62, 101.42, 101.71
α, β, γ (°)	90.0, 90.19, 90.0	91.9, 108.7, 108.2
Resolution (Å)	48.5–3.0 (3.05–3.00)[a]	95.3–3.6 (3.7–3.6)[a]
R_{merge}	0.073 (0.596)	0.117 (0.497)
$I/\sigma(I)$	11.8 (1.8)	7.5 (2.7)
$CC_{1/2}$	0.997 (0.733)	0.972 (0.597)
Completeness (%)	99.9 (98.7)	96.9 (97.1)
Redundancy	3.8 (3.8)	3.3 (3.4)
Refinement		
Resolution (Å)	48.5–3.0	45.7–3.6
No. reflections	107,485	26,956
R_{work}/R_{free}	0.221/0.251	0.217/0.257
No. atoms		
Protein	31,852	15,862
DNA	615	794
K^+	0	10
B factors		
Protein	78	121
DNA	90	143
K^+	–	118
RMS deviations		
Bond lengths (Å)	0.003	0.002
Bond angles (°)	0.571	0.480

Table 1. Summary of Data Collection and Refinement Statistics
One crystal was used for each structure.
RMS, root mean square.
[a]Values in parentheses are for highest-resolution shell.

electrostatic interactions with ssDNA (Kagawa et al., 2002; Singleton et al., 2002). Inside the groove, the distances between the side chain amino or guanidinium groups of Lys152, Arg153, and Arg156 and the phosphate backbone of the ssDNA were between 2.3 and 3.3 Å, indicating direct interactions between these residues and the ssDNA (Figure 1E).

The oligomerization state of the RAD52 ring was unaffected by ssDNA binding. Like the DNA-unbound RAD52, the DNA-bound RAD52 rings contained 11 subunits. The main chain conformations of the DNA-bound and DNA-unbound forms of RAD52 were also quite similar to each other (Figure S2A). The root-mean-square deviation (RMSD) was 0.538 Å for the superimposed RAD52 structures. The largest Cα to Cα distances were observed in the β-hairpin region (amino acid residues 53–65) (Figure S2B). These
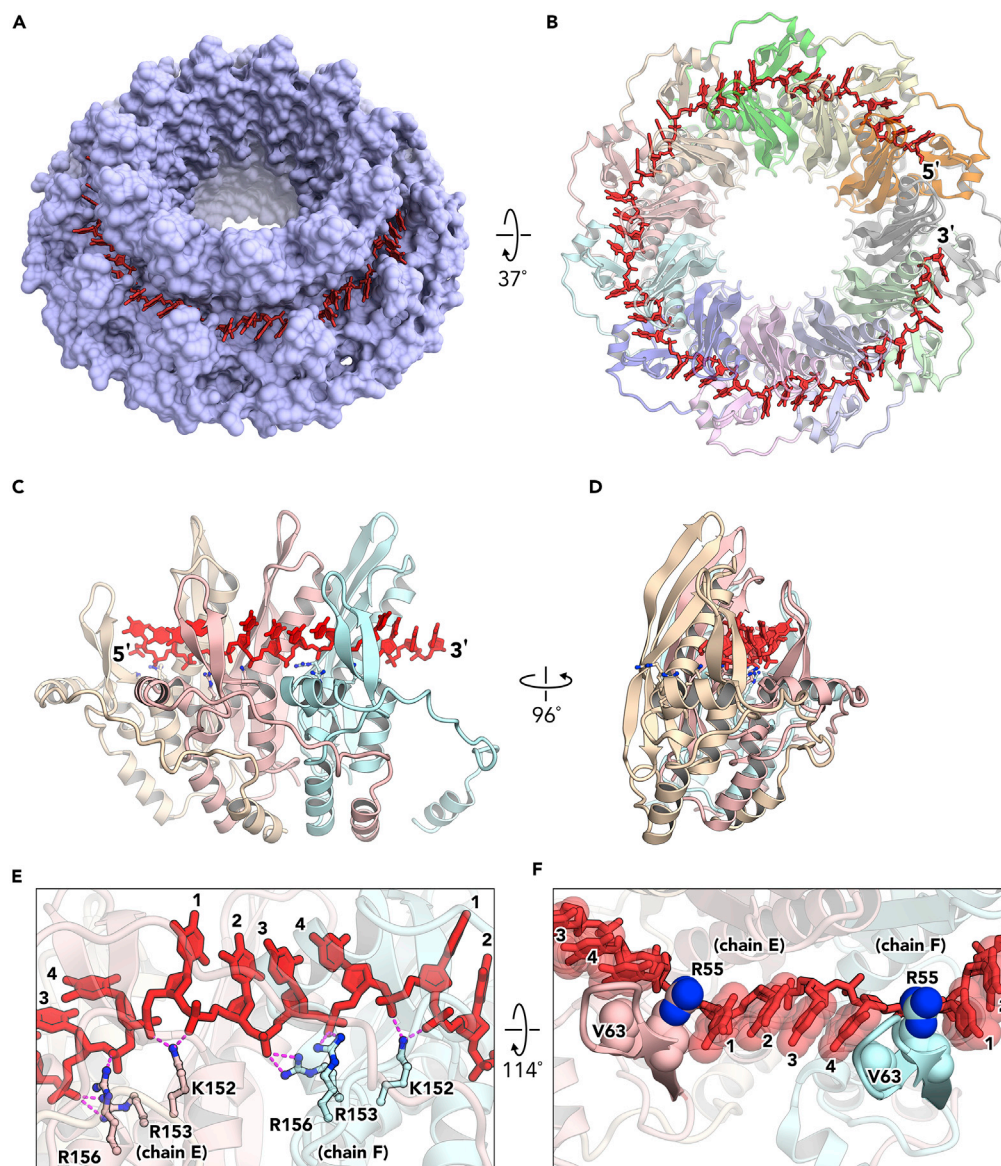
Figure 1. "Wrapped" Configuration of the ssDNA Around the Oligomeric RAD52 Ring

(A) Side view of the RAD52-ssDNA complex. To clearly depict the inner DNA binding site, the oligomeric RAD52 ring is shown in a surface representation (light blue). The ssDNA (red stick representation) is bound deeply within the cleft of RAD52 and occupies most of the space inside the groove.

(B) The RAD52-ssDNA complex, viewed down the central channel of the ring. The 40-nucleotide ssDNA (5' to 3' counterclockwise orientation) spans across 10 RAD52 subunits. Each subunit is colored differently.

(C and D) Two views of three consecutive RAD52 subunits and the 12-nucleotide ssDNA region that spans the subunits.

(E) A close-up view of the electrostatic interactions of K152, R153, and R156 with the phosphate backbone of the ssDNA. Dashed lines (magenta) depict potential hydrogen bonds.

(F) Hydrophobic stacking interactions that sandwich the four-nucleotide repeats. The β-hairpin structure of RAD52 (amino acid residues 52–66) is located between the four-nucleotide repeats. The ssDNA bases are sandwiched between R55 and V63 of the β-hairpin. For clarity, the DNA bases and the side chains of R55 and V63 are shown in sphere representations. See also Figures S1 and S2.

observations suggest that the DNA binding groove formed by the RAD52 ring is in a "ready state" for ssDNA binding, in which ssDNA can be accommodated without large conformational changes in the ring structure.
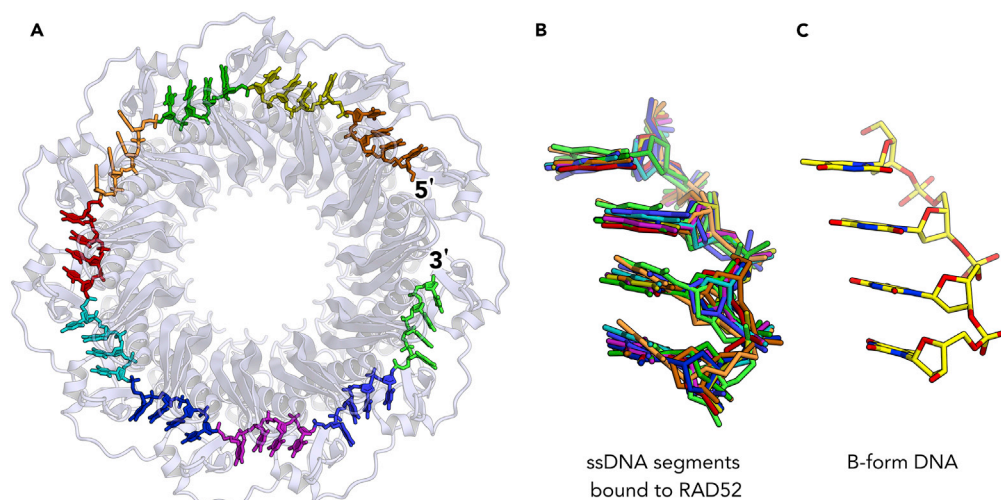
Figure 2. Conformation of the ssDNA Bound to the Inner DNA Binding Site

(A) The RAD52-ssDNA complex, viewed down the central channel of the ring. The four-nucleotide repeats in the 40-nucleotide ssDNA are colored differently.

(B) Superimposed structures of the ssDNA repeating units depicted in (A).

(C) Ideal B-form DNA.

See also Figure S3.

B-Form-like Structure of the ssDNA

The ssDNA bound to RAD52 exhibited a periodic structure along the entire length, with a stretched phosphate backbone region appearing every four nucleotides (Figure 2A). The four bases between the stretched regions had similar conformations to each other (Figure 2B). These structural features are consistent with the four-base periodicity observed in the previous hydroxyl radical footprinting studies of ssDNA bound to RAD52 (Singleton et al., 2002; Parsons et al., 2000). Interestingly, the DNA conformation of the four consecutive nucleotides between the stretched phosphate backbone was close to B-form (Figures 2B, 2C, and S3). The bases of the B-form-like segments of the ssDNA were sandwiched between Arg55 and Val63, likely by hydrophobic stacking interactions (Figure 1F). In particular, Arg55 straddled the stretched region of the phosphate backbone and appeared to anchor the ssDNA to the inner DNA binding site. Thus these residues seem to stabilize the B-form-like conformation of the ssDNA through hydrophobic stacking interactions with its bases.

We also found spherical electron densities near the stretched regions of the phosphate backbone (Figure 3A). These electron densities are probably derived from either potassium or calcium ions, because they were present in relatively high concentrations during the crystallization of the complex (25 mM potassium ion and 50 mM calcium ion). Potassium ions were modeled in the final complex structure, based on the fact that the average distance between the putative metal ion and the side chain oxygen atom of the nearest interacting amino acid residue (Glu140) was close to those reported for the coordinated potassium ion (Figure 3B; Zheng et al., 2008; Zheng et al., 2017). The putative metal ion was also in close proximity to the phosphate backbone of the ssDNA and the acidic residues, Glu145 and Asp149, of RAD52, and appeared to bridge the interaction between the two. The observed interaction between the putative metal ions, ssDNA, and RAD52 may explain the elevated ssDNA binding activities of RAD52 previously observed in the presence of divalent ions (Benson et al., 1998; Brouwer et al., 2017).

Structure of ssDNA Bound to the Outer DNA Binding Site of RAD52

We next determined the crystal structure of a RAD52-ssDNA complex, in which the ssDNA is bound to the outer DNA binding site. The crystal structure revealed a "trapped" ssDNA segment between two RAD52 rings (Figures 4A and 4B). The ssDNA had a markedly different structure from that bound to the inner DNA binding site. The ssDNA was mostly buried between the two RAD52 rings and formed a compact, right-handed helix containing intra-strand base-backbone contacts (Figures 4C and S4A–S4C). Consistent with a previous alanine-scanning mutagenesis study (Kagawa et al., 2008), Lys102 and Lys133 were the
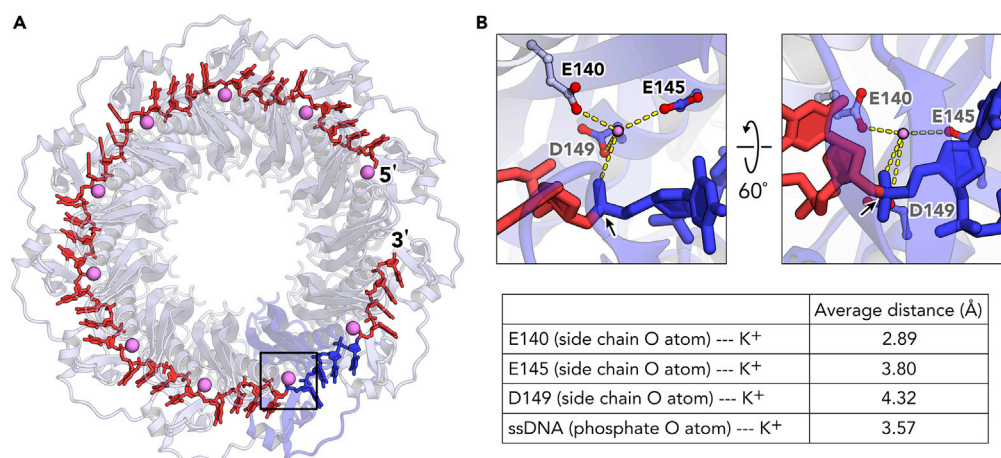
Figure 3. Putative Metal Ions Located between the Four-Nucleotide Repeats

(A) Locations of the putative metal ions (pink).

(B) Close-up views of the putative metal ion environment (boxed region) in (A). The putative metal ion (potassium ion) is surrounded by E140, E145, D149, and the phosphate group of the ssDNA (indicated with arrows). The table below shows the distances between the potassium ion and the potential coordinating ligands (side chain oxygen atoms from the acidic amino acid residues or oxygen atoms from the phosphate backbone of the ssDNA). The distances are averages over the 10 potassium ion-ligand interaction sites.

primary residues outside of the inner DNA binding site that were involved in the interactions with the ssDNA (Figures S4D–S4F).

A notable feature of the crystal structure is the close association between the RAD52 rings. The "trapped" ssDNA brings the DNA binding surfaces of the two RAD52 rings in close proximity (Figure 4A, schematic diagram). This results in a *trans* interaction between the β-hairpin (β1 and β2, Figure S2B) of one RAD52 ring and the outer DNA binding site (loop region between β3 and β4; loop region between β5 and α3, Figure S2B) of the second RAD52 ring. The associated region forms a confined space that includes both the inner and outer DNA binding sites and may provide a platform for DNA annealing. These structural features suggest a role of the outer DNA binding site in facilitating ring-ring associations on ssDNA.

In the crystal, a similar ring-ring association was observed between neighboring, symmetry-related RAD52-ssDNA complexes (Figures S5A and S5B). On each RAD52 ring, four "trapped" ssDNA segments with lengths ranging from 6 to 10 nucleotides were observed (Figure S5C). These interactions extend throughout the crystal, resulting in a RAD52-ssDNA network (Figure S5B). The observed crystal packing interactions may reflect the ability of RAD52 to effectively nucleate on ssDNA, as observed in previous electron micrographic studies of RAD52-ssDNA complexes (Van Dyck et al., 1998, 2001; Kagawa et al., 2001).

ssDNA Aggregation Promoted by the Outer DNA Binding Site

The "trapped" configuration of the ssDNA between two RAD52 rings suggests a role of the outer DNA binding site in promoting the accumulation of multiple RAD52 rings on ssDNA. To examine whether RAD52 aggregation on ssDNA is dependent on the outer DNA binding site, we incubated different concentrations of wild-type RAD52 or the K102A mutant with a circular ssDNA (ΦX174; 5,386 bases) and then centrifuged and analyzed the amounts of ssDNA in the upper and lower fractions of the centrifuged sample (Figure 5A). We found that as the concentration of the wild-type RAD52 increased, the amount of ssDNA in the lower fraction increased, indicating that a large network of RAD52-ssDNA complexes formed (Figure 5B). By contrast, the amounts of ssDNA in the upper and lower fractions of the centrifuged sample were nearly the same for the K102A mutant, regardless of the protein concentration (Figure 5C). The K102A mutant retained both ssDNA and dsDNA binding activities (Figure S6), indicating that the absence of aggregation activity was not because the mutant was completely defective in binding to DNA. These results suggest that the outer DNA binding site promotes the co-aggregation of RAD52 and ssDNA. Previously, we demonstrated that alanine substitutions of Lys102 and Lys133 impair the ability of RAD52 to promote
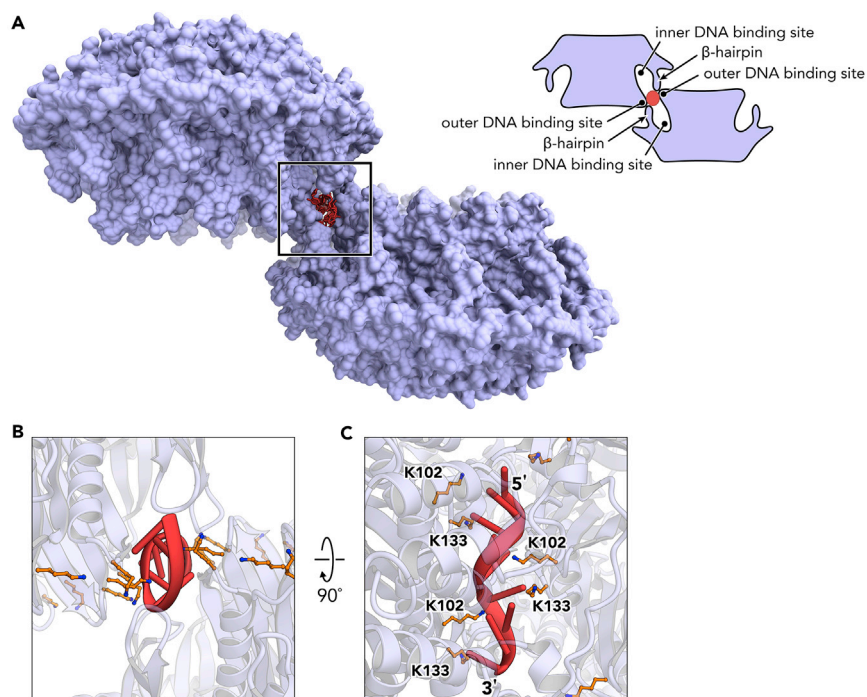
Figure 4. "Trapped" Configuration of ssDNA between Two RAD52 Rings

(A) Crystal structure of ssDNA bound to the outer DNA binding site of RAD52. The ssDNA (red) is "trapped" between two RAD52 rings (shown in a light blue surface representation). A schematic diagram of the complex is shown in the upper right.

(B and C) Close-up views of the ssDNA (boxed region) in (A). The helical structure of the ssDNA is stabilized by K102 and K133, which associate with the helical groove of the ssDNA.

See also Figures S4 and S5.

DNA annealing (Kagawa et al., 2008). Thus RAD52-mediated DNA annealing likely involves the aggregation of multiple RAD52 rings on ssDNA, which is promoted by the outer DNA binding site.

ssDNA Binding Affinities of the Two DNA Binding Sites

To further characterize the inner and outer DNA binding sites of RAD52, we investigated the ssDNA binding affinities of each site, using isothermal titration calorimetry (ITC). The K133A mutant, which contains a mutation in the outer DNA binding site, was utilized to determine the ssDNA binding affinity of the inner DNA binding site (Figure 6A). Similarly, the R55A/K152A mutant, which contains two mutations in the inner DNA binding site, was utilized to determine the ssDNA binding affinity of the outer DNA binding site (Figure 6B). The ITC experiments were performed by titrating a 40-mer ssDNA oligonucleotide into solutions of the mutant proteins. Analysis of the data revealed strikingly different thermodynamic profiles between the two mutants (Table S1). Heat absorption was observed for the K133A mutant (endothermic reaction; $\Delta H > 0$), whereas heat release was observed for the R55A/K152A mutant (exothermic reaction; $\Delta H < 0$). These results suggest that the ssDNA binding modes of the two sites are different, a conclusion that is consistent with the structures of the RAD52-ssDNA complexes.

The apparent dissociation constant (K_d) of the complex between the R55A/K152A mutant and ssDNA (~200 nM) was significantly lower than that of the K133A mutant (~24,000 nM). This indicates that the outer DNA binding site has higher affinity for ssDNA than the inner DNA binding site. To examine whether the two DNA binding sites interact with ssDNA in an independent or cooperative manner, we next performed an ITC experiment using the RAD52 protein without mutations. Like the K133A mutant, the RAD52 protein without mutations exhibited an initial, endothermic phase, which was indicative of ssDNA binding to the inner site (Figure 6C). However, RAD52 displayed a higher affinity toward ssDNA (~6 nM). This result suggests that the outer DNA binding site facilitated the ssDNA binding at the inner site. Thus in the initial endothermic phase, the ssDNA probably bound to both the inner and outer DNA
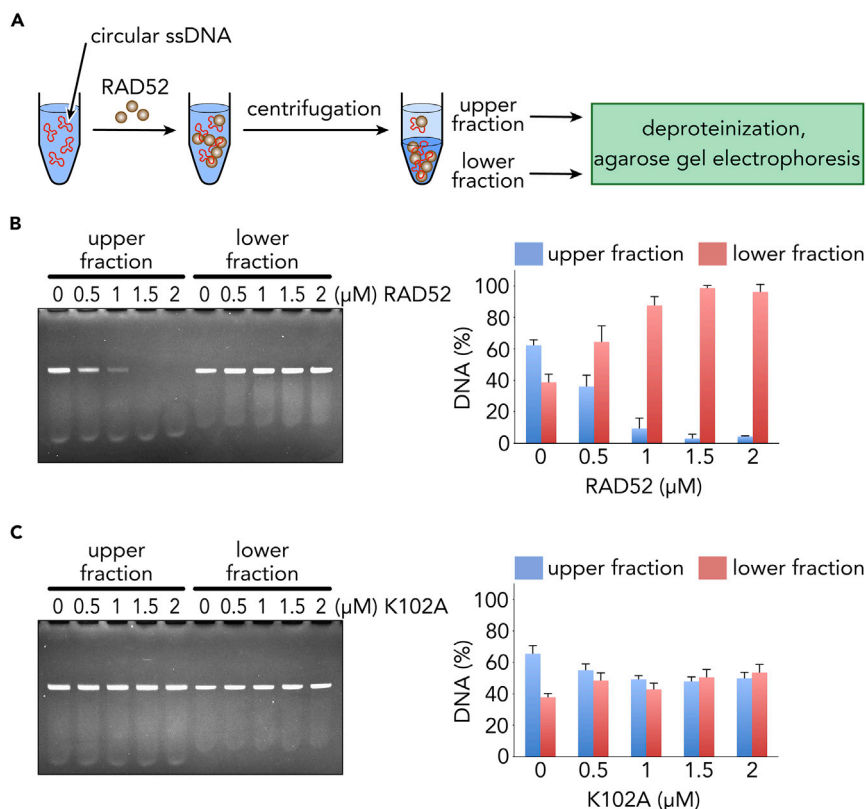
Figure 5. Accumulation of the Full-Length RAD52 Protein on ssDNA Is Promoted by the Outer DNA Binding Site
(A) A schematic diagram of the assay for examining the ssDNA aggregation promoted by the full-length RAD52.
(B and C) ssDNA aggregation activities of the wild-type and the mutant RAD52 (K102A). A circular, plasmid-sized ssDNA
(ΦX174, 5,386 bases) was used as the DNA substrate. The ssDNA was fractionated by agarose gel electrophoresis and
visualized by ethidium bromide staining. Error bars indicate standard deviations.
See also Figure S6.

binding sites, where the sum of the binding heats is predominantly endothermic. Moreover, the outer DNA binding site may be the initial contact site for ssDNA. Our findings demonstrate that the inner and outer binding sites cooperatively interact with ssDNA, which is likely important for the DNA annealing mediated by RAD52.

DISCUSSION

The crystal structures of the two RAD52-ssDNA complexes revealed how the two DNA binding sites may participate in RAD52-mediated DNA annealing. Both structures are compatible with the proposed model for SSA, in which RAD52 binds to resected DSBs (Van Dyck et al., 2001). The ssDNA bound to the inner DNA binding site was B-form-like, with the base-pairing edges of the bases exposed to the solvent. This conformation appears well suited for a homology search and base pair formation with a second ssDNA. By contrast, the ssDNA bound to the outer DNA binding site formed a compact, helical structure, and was buried at the ring-ring interface of RAD52. This interaction may be important for promoting ring-ring associations on ssDNA, thereby increasing the local concentration of RAD52 rings on ssDNA.

Collectively, the two crystal structures and the various analyses presented here help to define a framework for understanding how RAD52 promotes DNA annealing (Figure 7). In our proposed model, RAD52 would initially contact the ssDNA at the outer DNA binding site. Our ITC experiments revealed that the outer binding site has higher affinity for ssDNA than the inner binding site. The "trapped" configuration would promote the accumulation of multiple RAD52 rings on both complementary ssDNAs. This is consistent with the previous report of the accumulation of RAD52 at DSBs, in an ionizing radiation-dependent manner
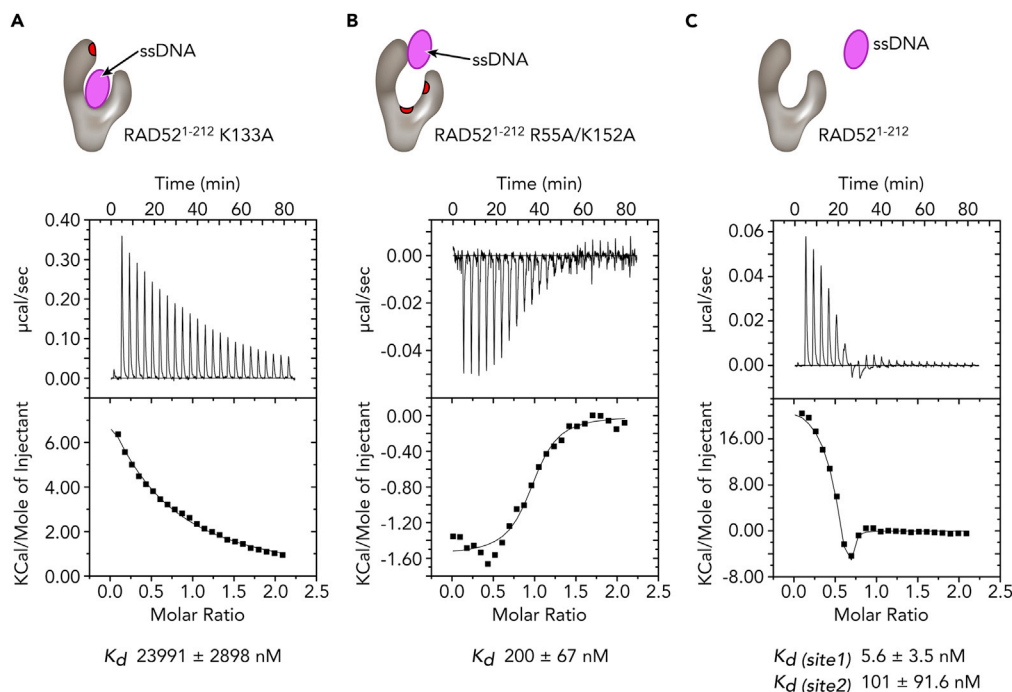
Figure 6. ITC Isotherms for the Binding of ssDNA to RAD52

The upper panel shows the raw titration data, plotted as the heat signal (microcalories per second) versus time (minutes), obtained for 24 injections (12 μL each) of the 40-mer ssDNA oligonucleotide (polydeoxythymine) into a solution containing RAD52. The lower panel shows the ITC data from the upper panel in the form of a titration isotherm, where the integrated heat responses per injection were normalized to the moles of injected ssDNA and plotted versus the total ssDNA to 11-mer RAD52 ratio. The red patches on the schematic diagrams of the RAD52 subunits indicate the mutation sites.

(A) Calorimetric titration of ssDNA (200 μM) into the RAD52$^{1-212}$ K133A mutant (20 μM 11-mer). The continuous curve depicts the best fit of the data to a one-site model.

(B) Calorimetric titration of ssDNA (100 μM) into the RAD52$^{1-212}$ R55A/K152A mutant (10 μM 11-mer). The continuous curve depicts the best fit of the data to a one-site model.

(C) Calorimetric titration of ssDNA (100 μM) into RAD52$^{1-212}$ (10 μM 11-mer). The continuous curve depicts the best fit of the data to a two-site model.

See also Table S1.

(Wray et al., 2008). At some point, the "trapped" ssDNA would move into the inner DNA binding site, where the conformation becomes B-form. The ssDNA bound to RAD52 would then undergo a homology search with another ssDNA bound to a different RAD52 ring (Rothenberg et al., 2008; Grimme et al., 2010), either by random collision or through directional movement. The B-form conformation induced in the bound ssDNA would facilitate the homology search. When homology is found, the inner DNA binding site would release the base-paired regions of the ssDNA. We previously reported that the outer DNA binding site displays dsDNA binding activity and introduces positive supercoils into dsDNA (Kagawa et al., 2008). Thus after homology has been found, the paired ssDNA region may move to the outer DNA binding sites of the RAD52 rings that promoted the base pair formation, or bind to the outer DNA binding site of a different pair of RAD52 rings, where the duplex DNA would be stabilized.

The structure of the RAD52-ssDNA complex and the proposed mechanism for RAD52-mediated DNA annealing share several key features to those of the bacterial DdrB, the only SSA protein for which high-resolution insight into the mechanism of protein-assisted DNA annealing is currently available (Sugiman-Marangos et al., 2016). Like RAD52, DdrB forms a homo-multimeric ring structure, and accommodates ssDNA around the ring structure. The ssDNAs bound to RAD52 and DdrB are oriented such that the bases are accessible to the incoming homologous DNA strand. The two proteins are also similar in that the proposed models for DNA annealing involve the interface between two multimeric ring structures. RAD52 and DdrB also exhibit some differences, such as the number of ssDNA bases bound to each subunit and the ring
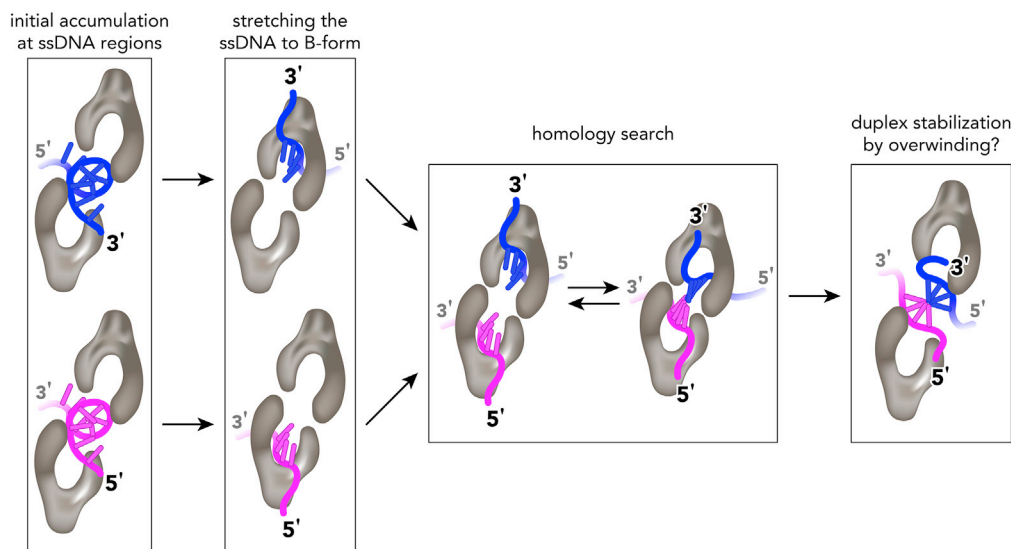
Figure 7. A Model for RAD52-Mediated DNA Annealing

Close-up views of the RAD52-ssDNA interactions leading to the homology search. Initially, both cDNA strands (colored blue and magenta) are "trapped" by RAD52 rings. The ssDNA moves into the inner DNA binding site of either one of the RAD52 rings that is "trapping" the ssDNA, based on the 5' to 3' orientation. The magenta-colored ssDNA is bound to the bottom RAD52 ring, whereas the blue-colored ssDNA is bound to the top RAD52 ring. The RAD52 rings accommodating the ssDNA associate with each other to facilitate the homology search.

See also Figures S7 and S8.

orientations in the multi-ring complex. These differences may reflect the distinct mechanisms utilized by each protein. Nevertheless, the present findings appear consistent with previous observations of other SSA proteins. Thus the proposed DNA annealing model is probably valid for ancestors of RAD52 in lower organisms and bacteriophages, such as the Sak protein from the *Lactobacillus lactis* phage ul36 (Ploquin et al., 2008; Scaltriti et al., 2010).

We note that the four-nucleotide, B-form-like segment of the ssDNA bound to the inner DNA binding site is not fully accessible for base pairing with the cDNA strand, owing to steric clashes between the complementary strand and the inner walls of the DNA binding groove (Figures S7A–S7C). We speculate that, during the search for DNA homology, the ssDNA bound to the inner DNA binding site detaches from the bottom of the groove, to make the bases more accessible for base pairing (Figure S7D). This could be facilitated if Arg55, which appears to act as an entry/exit gate for ssDNA, "opens" so that it no longer straddles the phosphate backbone of the ssDNA. The "opening" of the Arg55 gate may result from conformational changes in the β-hairpin, when the DNA binding sites of two RAD52 rings come in close contact.

Importantly, the present structural findings are consistent with the DNA annealing activities displayed by the various point mutants of full-length RAD52 (Figure S8). Alanine substitutions of amino acid residues at the inner and outer DNA binding sites (Lys102, Lys133, Lys152, Arg153, and Arg156), which are important for the stable association with ssDNA, significantly impaired the ability of RAD52 to efficiently promote the annealing of complementary 50-mer oligonucleotides (Figures S8B and S8D). By contrast, the alanine substitution of Arg55 resulted in a milder defect in DNA annealing (Figure S8C), when compared with those of Lys152, Arg153, and Arg156, implying that Arg55 may have a distinct role in DNA annealing. This observation is consistent with the unique role of Arg55 revealed by the present structural studies. The amino acid residues that constitute the two DNA binding sites are well conserved among RAD52 orthologs (Figure S8E), suggesting that the mechanisms to promote DNA annealing are also conserved.

Intriguingly, the mechanisms to induce the B-form-like conformation of ssDNA do not appear to be specific to RAD52. The B-form-like conformation of the ssDNA was stabilized by the electrostatic interactions between the phosphate backbone and the basic residues at the bottom of the DNA binding groove, as well as

by the hydrophobic stacking interactions between the ssDNA bases and the Arg55 and Val63 residues of the β-hairpin. The latter hydrophobic interaction resulted in a stretched phosphate backbone conformation (with respect to B-form) and the sandwiching of four consecutive bases. The stretching of the phosphate backbone and the sandwiching of bases are also observed in the ssDNA structure bound to the bacterial RecA recombinase (Chen et al., 2008), which lacks apparent sequence homology to RAD52 and exhibits a completely different oligomerization structure. Thus the stretching and sandwiching may be common interaction modes utilized by proteins that expose the base pairing edges of ssDNA to the solvent, to facilitate base pair formation with a cDNA strand.

In summary, the crystal structures of the RAD52-ssDNA complexes revealed in this study are important for understanding the molecular mechanisms of HDR systems, especially those that do not involve RAD51. Several types of cancers have defects in the genes that function in RAD51-dependent HDR pathways, such as BRCA1, BRCA2, and PALB2. RAD52 is synthetically lethal with these genes (Feng et al., 2011; Lok et al., 2013), suggesting that RAD52 is a potential target for cancer therapeutics (O'Connor, 2015). The present complex structures may be useful in designing inhibitors that target RAD52 for cancer treatment.

METHODS

All methods can be found in the accompanying Transparent Methods supplemental file.

SUPPLEMENTAL INFORMATION

Supplemental Information includes Transparent Methods, eight figures, and one table and can be found with this article online at https://doi.org/10.1016/j.isci.2018.04.005.

ACKNOWLEDGMENTS

AUTHOR CONTRIBUTIONS

Conceptualization, W.K. and H.K.; methodology, M.S., K.S., and W.K.; investigation, M.S., K.S., S.S., H.O., and W.K.; writing: original draft, W.K. and M.S.; writing: review and editing, W.K., H.K., M.S., K.S., T.Y., H.O., and Y.N.; supervision, W.K.; funding acquisition, W.K., H.K., and Y.N.

DECLARATION OF INTERESTS

The authors declare no competing interests.

SUPPORTING CITATIONS

The following references appear in the Supplemental Information: Adams et al., 2010; Battye et al., 2011; Brünger et al., 1998; Brünger, 2007; Chen et al., 2010; Emsley et al., 2010; Gasteiger et al., 2005; Goujon et al., 2010; Kabsch, 2010; Lu and Olson, 2003; McCoy et al., 2007; Saotome et al., 2016; Schneider et al., 2012; Sievers et al., 2011; Terwilliger, 2000; Winn et al., 2011.

iScience

CellPress

REFERENCES

Adams, P.D., Afonine, P.V., Bunkóczi, G., Chen, V.B., Davis, I.W., Echols, N., Headd, J.J., Hung, L.W., Kapral, G.J., Grosse-Kunstleve, R.W., et al. (2010). PHENIX: a comprehensive Python-based system for macromolecular structure solution. Acta Crystallogr. D Biol. Crystallogr. 66, 213–221.

Battye, T.G.G., Kontogiannis, L., Johnson, O., Powell, H.R., and Leslie, A.G.W. (2011). iMosflm: a new graphical interface for diffraction-image processing with MOSFLM. Acta Crystallogr. D Biol. Crystallogr. 67, 271–281.

Benson, F.E., Baumann, P., and West, S.C. (1998). Synergistic actions of Rad51 and Rad52 in recombination and DNA repair. Nature 391, 401–404.

Bhargava, R., Onyango, D.O., and Stark, J.M. (2016). Regulation of single-strand annealing and its role in genome maintenance. Trends Genet. 32, 566–575.

Bhowmick, R., Minocherhomji, S., and Hickson, I.D. (2016). RAD52 facilitates mitotic DNA synthesis following replication stress. Mol. Cell 64, 1117–1126.

Brouwer, I., Zhang, H., Candelli, A., Normanno, D., Peterman, E.J.G., Wuite, G.J.L., and Modesti, M. (2017). Human RAD52 captures and holds DNA strands, increases DNA flexibility, and prevents melting of duplex DNA: implications for DNA recombination. Cell Rep. 18, 2845–2853.

Brünger, A.T., Adams, P.D., Clore, G.M., DeLano, W.L., Gros, P., Grosse-Kunstleve, R.W., Jiang, J.-S., Kuszewski, J., Nilges, M., Pannu, N.S., et al. (1998). Crystallography & NMR system: a new software suite for macromolecular structure determination. Acta Crystallogr. D Biol. Crystallogr. 54, 905–921.

Brünger, A.T. (2007). Version 1.2 of the crystallography and NMR system. Nat. Protoc. 2, 2728–2733.

Ceccaldi, R., Rondinelli, B., and D'Andrea, A.D. (2016). Repair pathway choices and consequences at the double-strand break. Trends Cell Biol. 26, 52–64.

Chen, V.B., Arendall, W.B., Headd, J.J., Keedy, D.A., Immormino, R.M., Kapral, G.J., Murray, L.W., Richardson, J.S., and Richardson, D.C. (2010). MolProbity: all-atom structure validation for macromolecular crystallography. Acta Crystallogr. D Biol. Crystallogr. 66, 12–21.

Chen, Z., Yang, H., and Pavletich, N.P. (2008). Mechanism of homologous recombination from the RecA-ssDNA/dsDNA structures. Nature 453, 489–494.

Ciccia, A., and Symington, L.S. (2016). Stressing out about RAD52. Mol. Cell 64, 1017–1019.

Emsley, P., Lohkamp, B., Scott, W.G., and Cowtan, K. (2010). Features and development of coot. Acta Crystallogr. D Biol. Crystallogr. 66, 486–501.

Feng, Z., Scott, S.P., Bussen, W., Sharma, G.G., Guo, G., Pandita, T.K., and Powell, S.N. (2011). Rad52 inactivation is synthetically lethal with BRCA2 deficiency. Proc. Natl. Acad. Sci. USA 108, 686–691.

Game, J.C., and Mortimer, R.K. (1974). A genetic study of X-ray sensitive mutants in yeast. Mutat. Res. 24, 281–292.

Gasteiger, E., Hoogland, C., Gattiker, A., Duvaud, S., Wilkins, M.R., Appel, R.D., and Bairoch, A. (2005). Protein identification and analysis tools on the ExPASy server. In The Proteomics Protocols Handbook, J.M. Walker, ed. (Humana Press), pp. 571–607.

Goujon, M., McWilliam, H., Li, W., Valentin, F., Squizzato, S., Paern, J., and Lopez, R. (2010). A new bioinformatics analysis tools framework at EMBL-EBI. Nucleic Acids Res. 38, W695–W699.

Grimme, J.M., Honda, M., Wright, R., Okuno, Y., Rothenberg, E., Mazin, A.V., Ha, T., and Spies, M. (2010). Human Rad52 binds and wraps single-stranded DNA and mediates annealing via two hRad52-ssDNA complexes. Nucleic Acids Res. 38, 2917–2930.

Hanamshet, K., Mazina, O.M., and Mazin, A.V. (2016). Reappearance from obscurity: mammalian Rad52 in homologous recombination. Genes (Basel) 7, 63.

Heyer, W., Ehmsen, K.T., and Liu, J. (2010). Regulation of homologous recombination in eukaryotes. Annu. Rev. Genet. 44, 113–139.

Ivanov, E.L., Sugawara, N., Fishman-Lobell, J., and Haber, J.E. (1996). Genetic requirements for the single-strand annealing pathway of double-strand break repair in Saccharomyces cerevisiae. Genetics 142, 693–704.

Jackson, S.P., and Bartek, J. (2009). The DNA-damage response in human biology and disease. Nature 461, 1071–1078.

Kabsch, W. (2010). XDS. Acta Crystallogr. D Biol. Crystallogr. 66, 125–132.

Kagawa, W., Kagawa, A., Saito, K., Ikawa, S., Shibata, T., Kurumizaka, H., and Yokoyama, S. (2008). Identification of a second DNA binding site in the human Rad52 protein. J. Biol. Chem. 283, 24264–24273.

Kagawa, W., Kurumizaka, H., Ikawa, S., Yokoyama, S., and Shibata, T. (2001). Homologous pairing promoted by the human Rad52 protein. J. Biol. Chem. 276, 35201–35208.

Kagawa, W., Kurumizaka, H., Ishitani, R., Fukai, S., Nureki, O., Shibata, T., and Yokoyama, S. (2002). Crystal structure of the homologous-pairing domain from the human Rad52 recombinase in the undecameric form. Mol. Cell 10, 359–371.

Krogh, B.O., and Symington, L.S. (2004). Recombination proteins in yeast. Annu. Rev. Genet. 38, 233–271.

Lieber, M.R. (2010). The mechanism of double-strand DNA break repair by the non-homologous DNA end-joining pathway. Annu. Rev. Biochem. 79, 181–211.

Lloyd, J.A., McGrew, D.A., and Knight, K.L. (2005). Identification of residues important for DNA binding in the full-length human Rad52 protein. J. Mol. Biol. 345, 239–249.

Lok, B.H., Carley, A.C., Tchang, B., and Powell, S.N. (2013). RAD52 inactivation is synthetically lethal with deficiencies in BRCA1 and PALB2 in addition to BRCA2 through RAD51-mediated homologous recombination. Oncogene 32, 3552–3558.

Lu, X.-J., and Olson, W.K. (2003). 3DNA: a software package for the analysis, rebuilding and visualization of three-dimensional nucleic acid structures. Nucleic Acids Res. 31, 5108–5121.

McCoy, A.J., Grosse-Kunstleve, R.W., Adams, P.D., Winn, M.D., Storoni, L.C., and Read, R.J. (2007). Phaser crystallographic software. J. Appl. Crystallogr. 40, 658–674.

Mehta, A., and Haber, J.E. (2014). Sources of DNA double-strand breaks and models of recombinational DNA repair. Cold Spring Harb. Perspect. Biol. 6, a016428.

Morrical, S.W. (2015). DNA-pairing and annealing processes in homologous recombination and homology-directed repair. Cold Spring Harb. Perspect. Biol. 7, a016444.

Mortensen, U.H., Bendixen, C., Sunjevaric, I., and Rothstein, R. (1996). DNA strand annealing is promoted by the yeast Rad52 protein. Proc. Natl. Acad. Sci. USA 93, 10729–10734.

Moynahan, M.E., and Jasin, M. (2010). Mitotic homologous recombination maintains genomic stability and suppresses tumorigenesis. Nat. Rev. Mol. Cell Biol. 11, 196–207.

New, J.H., Sugiyama, T., Zaitseva, E., and Kowalczykowski, S.C. (1998). Rad52 protein stimulates DNA strand exchange by Rad51 and replication protein A. Nature 391, 407–410.

O'Connor, M.J. (2015). Targeting the DNA damage response in cancer. Mol. Cell 60, 547–560.

Pâques, F., and Haber, J.E. (1999). Multiple pathways of recombination induced by double-strand breaks in Saccharomyces cerevisiae. Microbiol. Mol. Biol. Rev. 63, 349–404.

Parsons, C.A., Baumann, P., Van Dyck, E., and West, S.C. (2000). Precise binding of single-stranded DNA termini by human RAD52 protein. EMBO J. 19, 4175–4181.

Ploquin, M., Bransi, A., Paquet, E.R., Stasiak, A.J., Stasiak, A., Yu, X., Cieslinska, A.M., Egelman, E.H., Moineau, S., and Masson, J.-Y. (2008). Functional and structural basis for a bacteriophage homolog of human RAD52. Curr. Biol. 18, 1142–1146.

Ranatunga, W., Jackson, D., Lloyd, J.A., Forget, A.L., Knight, K.L., and Borgstahl, G.E. (2001). Human RAD52 exhibits two modes of self-association. J. Biol. Chem. 276, 15876–15880.

Reddy, G., Golub, E.I., and Radding, C.M. (1997). Human Rad52 protein promotes single-strand DNA annealing followed by branch migration. Mutat. Res. 377, 53–59.

Rothenberg, E., Grimme, J., Spies, M., and Ha, T. (2008). Human Rad52-mediated homology search and annealing occurs by continuous interactions

between overlapping nucleoprotein complexes. Proc. Natl. Acad. Sci. USA *105*, 20274–20279.

San Filippo, J., Sung, P., and Klein, H. (2008). Mechanism of eukaryotic homologous recombination. Annu. Rev. Biochem. *77*, 229–257.

Saotome, M., Saito, K., Onodera, K., Kurumizaka, H., and Kagawa, W. (2016). Structure of the human DNA-repair protein RAD52 containing surface mutations. Acta Crystallogr. F Struct. Biol. Commun. *72*, 598–603.

Scaltriti, E., Moineau, S., Launay, H., Masson, J.-Y., Rivetti, C., Ramoni, R., Campanacci, V., Tegoni, M., and Cambillau, C. (2010). Deciphering the function of lactococcal phage ul36 Sak domains. J. Struct. Biol. *170*, 462–469.

Schneider, C.A., Rasband, W.S., and Eliceiri, K. (2012). NIH Image to ImageJ: 25 years of image analysis. Nat. Methods *9*, 671–675.

Shinohara, A., and Ogawa, T. (1998). Stimulation by Rad52 of yeast Rad51-mediated recombination. Nature *391*, 404–407.

Shinohara, A., Shinohara, M., Ohta, T., Matsuda, S., and Ogawa, T. (1998). Rad52 forms ring structures and co-operates with RPA in single-strand DNA annealing. Genes Cells *3*, 145–156.

Sievers, F., Wilm, A., Dineen, D., Gibson, T.J., Karplus, K., Li, W., Lopez, R., McWilliam, H., Remmert, M., Söding, J., et al. (2011). Fast, scalable generation of high-quality protein multiple sequence alignments using Clustal Omega. Mol. Syst. Biol. *7*, 539.

Singleton, M.R., Wentzell, L.M., Liu, Y., West, S.C., and Wigley, D.B. (2002). Structure of the single-

strand annealing domain of human RAD52 protein. Proc. Natl. Acad. Sci. USA *99*, 13492–13497.

Song, B.W., and Sung, P. (2000). Functional interactions among yeast Rad51 recombinase, Rad52 mediator, and replication protein A in DNA strand exchange. J. Biol. Chem. *275*, 15895–15904.

Sotiriou, S.K., Kamileri, I., Lugli, N., Evangelou, K., Da-Ré, C., Huber, F., Padayachy, L., Tardy, S., Nicati, N.L., Barriot, S., et al. (2016). Mammalian RAD52 functions in break-induced replication repair of collapsed DNA replication forks. Mol. Cell *64*, 1127–1134.

Stasiak, A.Z., Larquet, E., Stasiak, A., Müller, S., Engel, A., Van Dyck, E., West, S.C., and Egelman, E.H. (2000). The human Rad52 protein exists as a heptameric ring. Curr. Biol. *10*, 337–340.

Sugiman-Marangos, S.N., Weiss, Y.M., and Junop, M.S. (2016). Mechanism for accurate, protein-assisted DNA annealing by *Deinococcus radiodurans* DdrB. Proc. Natl. Acad. Sci. USA *113*, 4308–4313.

Sugiyama, T., and Kowalczykowski, S.C. (2002). Rad52 protein associates with replication protein A (RPA)-single-stranded DNA to accelerate Rad51-mediated displacement of RPA and presynaptic complex formation. J. Biol. Chem. *277*, 31663–31672.

Sugiyama, T., New, J.H., and Kowalczykowski, S.C. (1998). DNA annealing by RAD52 protein is stimulated by specific interaction with the complex of replication protein A and single-stranded DNA. Proc. Natl. Acad. Sci. USA *95*, 6049–6054.

Sung, P. (1997). Function of yeast Rad52 protein as a mediator between replication protein A and the Rad51 recombinase. J. Biol. Chem. *272*, 28194–28197.

Terwilliger, T.C. (2000). Maximum likelihood density modification. Acta Crystallogr. D Biol. Crystallogr. *56*, 965–972.

Van Dyck, E., Hajibagheri, N.M., Stasiak, A., and West, S.C. (1998). Visualisation of human Rad52 protein and its complexes with hRad51 and DNA. J. Mol. Biol. *284*, 1027–1038.

Van Dyck, E., Stasiak, A.Z., Stasiak, A., and West, S.C. (2001). Visualisation of recombination intermediates produced by RAD52-mediated single-strand annealing. EMBO Rep. *2*, 905–909.

Winn, M.D., Ballard, C.C., Cowtan, K.D., Dodson, E.J., Emsley, P., Evans, P.R., Keegan, R.M., Krissinel, E.B., Leslie, A.G., McCoy, A., et al. (2011). Overview of the CCP4 suite and current developments. Acta Crystallogr. D Biol. Crystallogr. *67*, 235–242.

Wray, J., Liu, J., Nickoloff, J.A., and Shen, Z. (2008). Distinct RAD51 associations with RAD52 and BCCIP in response to DNA damage and replication stress. Cancer Res. *68*, 2699–2707.

Zheng, H., Chruszcz, M., Lasota, P., Lebioda, L., and Minor, W. (2008). Data mining of metal ion environments present in protein structures. J. Inorg. Biochem. *102*, 1765–1776.

Zheng, H., Cooper, D.R., Porebski, P.J., Shabalin, I.G., Handing, K.B., and Minor, W. (2017). CheckMyMetal: a macromolecular metal-binding validation tool. Acta Crystallogr. D Struct. Biol. *73*, 223–233.

Supplemental Information

Structural Basis of Homology-Directed

DNA Repair Mediated by RAD52

Mika Saotome, Kengo Saito, Takeshi Yasuda, Hideaki Ohtomo, Shusei Sugiyama, Yoshifumi Nishimura, Hitoshi Kurumizaka, and Wataru Kagawa
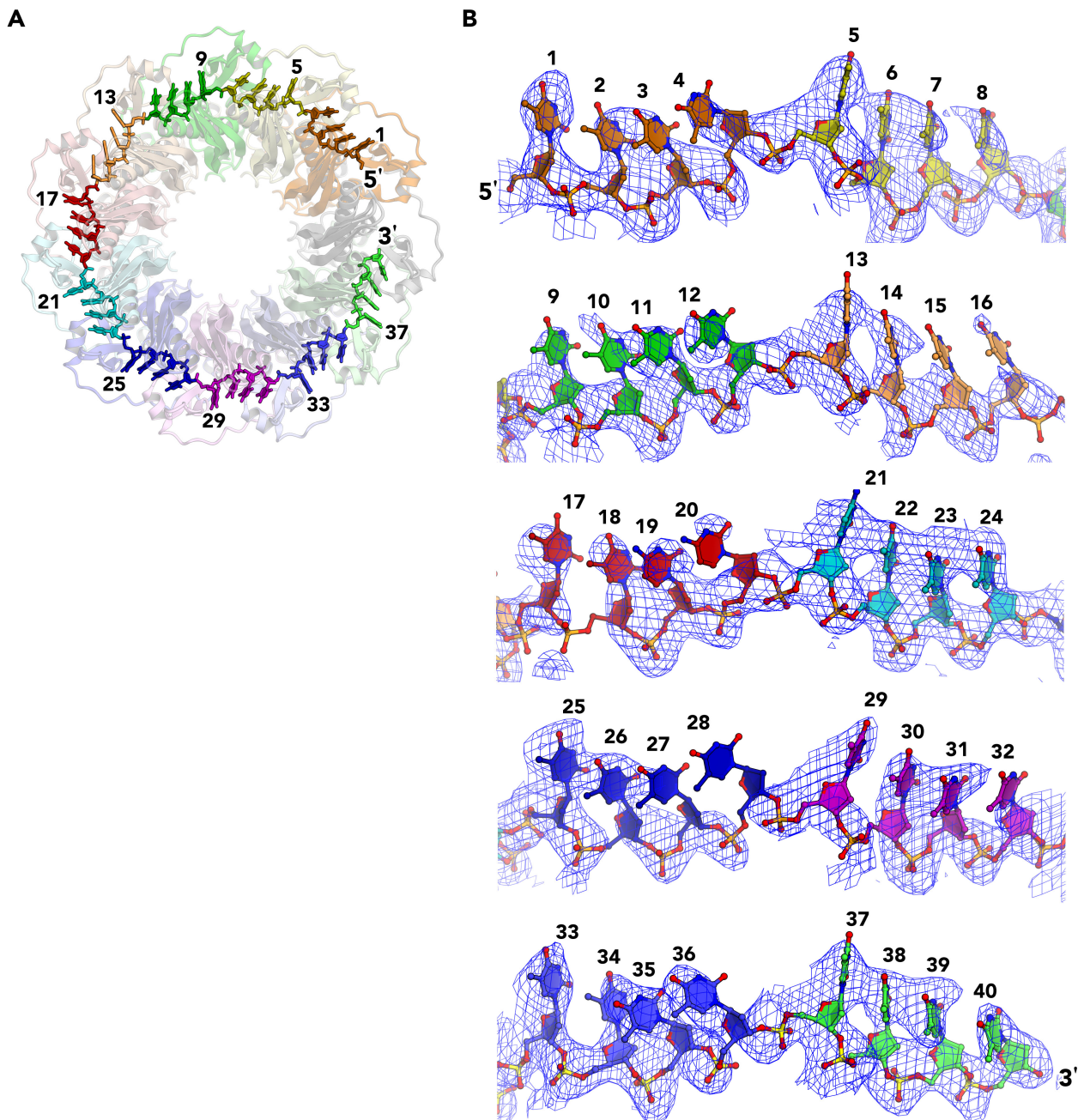
Figure S1. The Electron Density Maps of the ssDNA Bound to the Inner DNA Binding Site of RAD52, Related to Figure 1

(A) The entire 40-mer ssDNA bound to RAD52. Each four-nucleotide repeat is colored differently. The 5' and 3' ends are depicted.

(B) The *2mFo-DFc* composite omit maps (contoured at 1 σ) for every nucleotide are shown from the 5' to 3' end, in eight nucleotide blocks. The omit map was created using the "Composite omit map" tool in the *PHENIX* program (Adams et al., 2010).
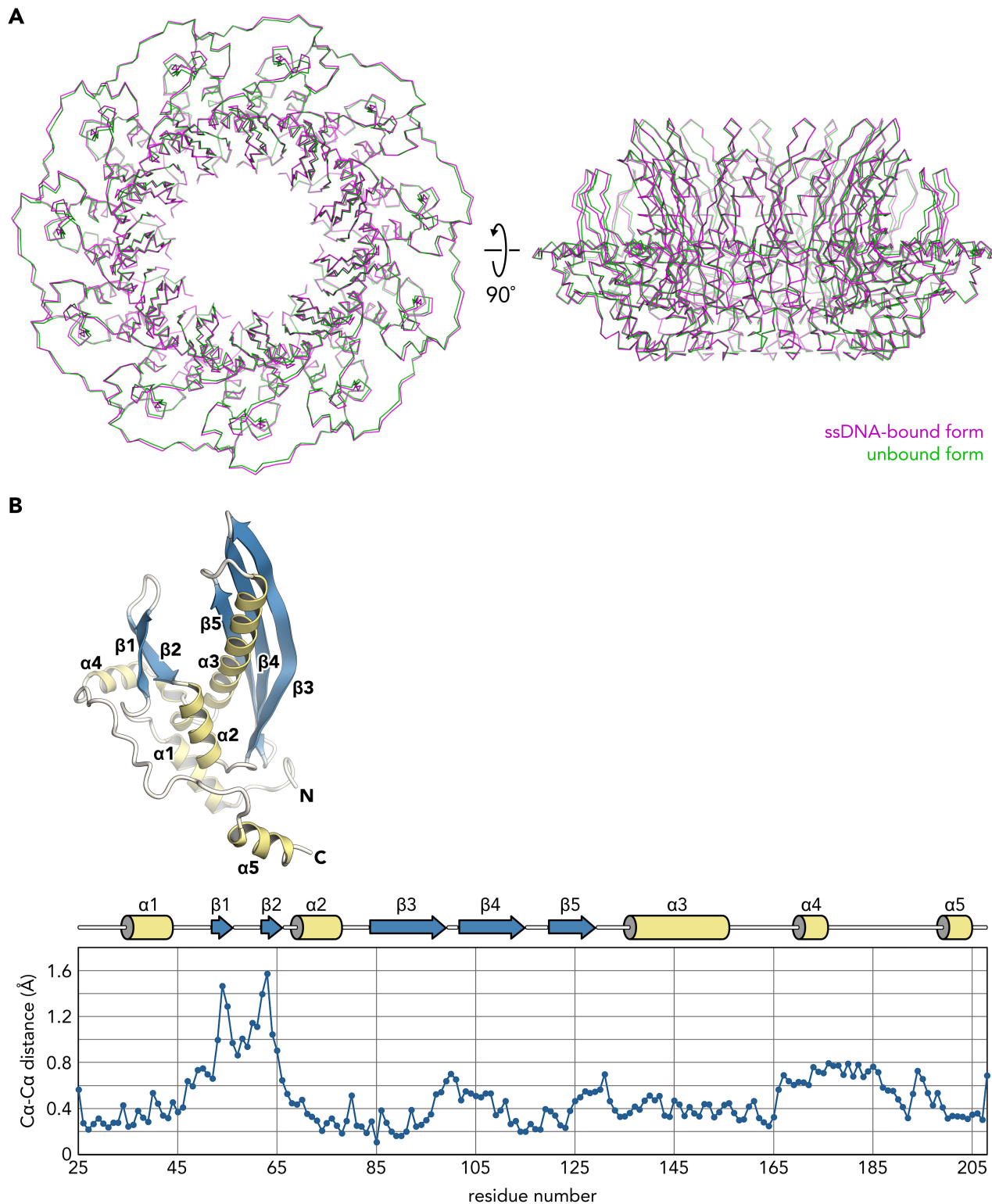
Figure S2. A Structural Comparison of the ssDNA-Bound and Unbound Forms of RAD52, Related to Figure 1

(A) Superimposed Cα traces of the ssDNA-bound (magenta; PDB: 5XRZ) and unbound (green; PDB: 1KN0) forms of the RAD52 undecameric ring. The "align" tool in *PyMOL* was used to superimpose

the two structures. The RMSD between the ssDNA-bound and unbound forms was calculated from 14,207 pairs of Cα atoms.

(B) The average distances between the corresponding Cα atoms of the superimposed RAD52 rings shown in (A). The secondary and tertiary structures are indicated above the graph for clarity.
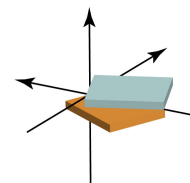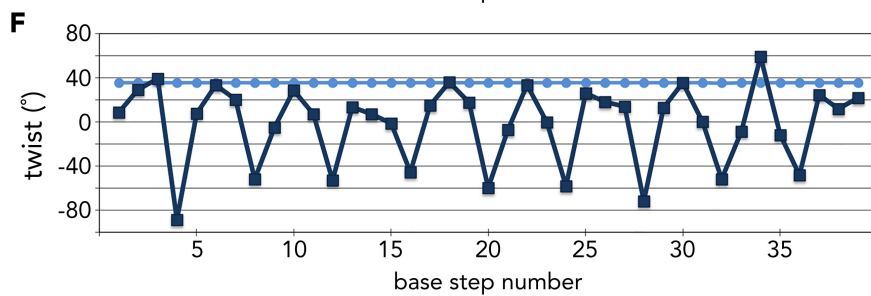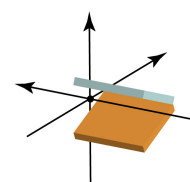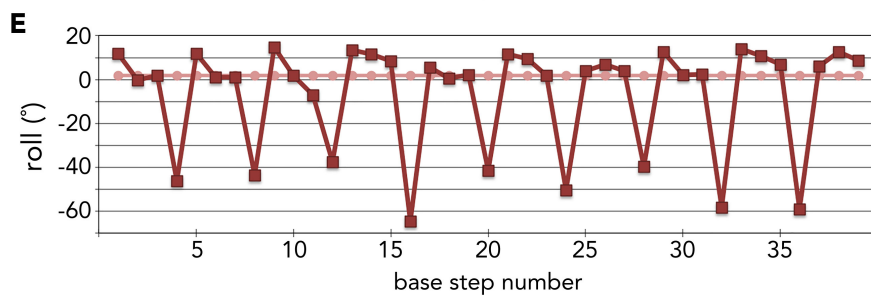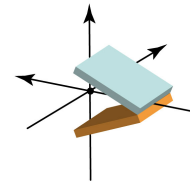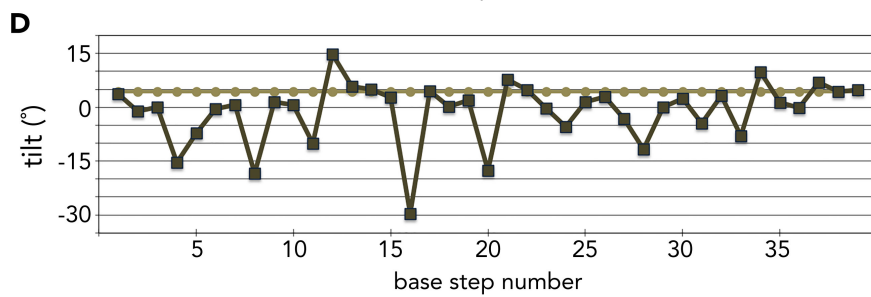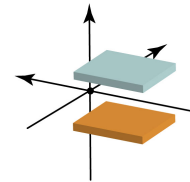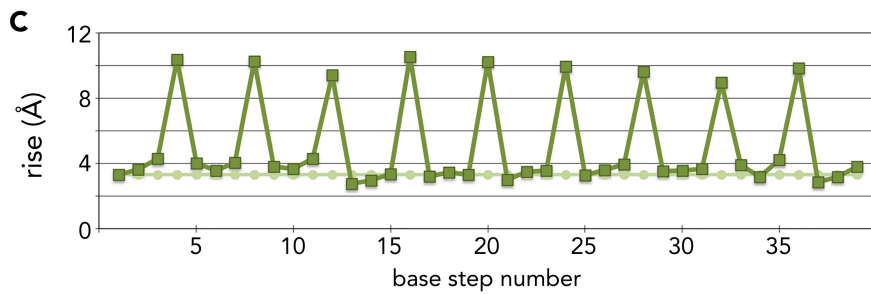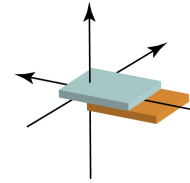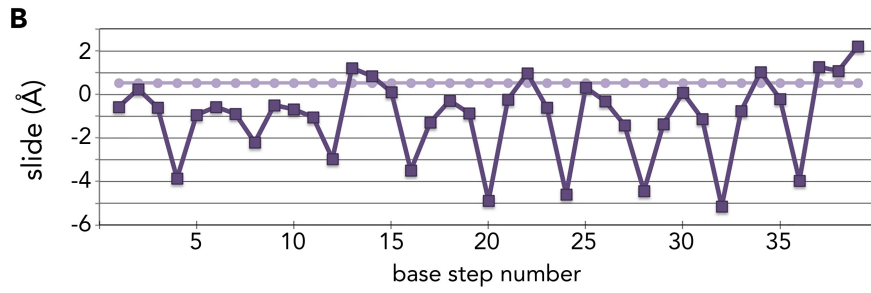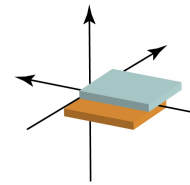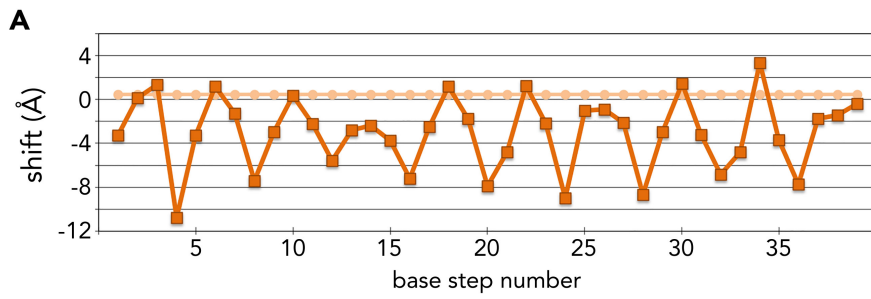
A shift (Å) vs base step number

B slide (Å) vs base step number

C rise (Å) vs base step number

D tilt (°) vs base step number

E roll (°) vs base step number

F twist (°) vs base step number

The base step parameters were calculated using the *3DNA* program (Lu and Olson, 2003), and compared with those of the ideal B-form DNA. The graph is colored differently for each parameter. The horizontal, light-colored line shown in each graph corresponds to the ideal B-form DNA. The base step number (n) indicates the base step between the nth base and the (n+1)th base.

(A) shift.

(B) slide.

(C) rise.

(D) tilt.

(E) roll.

(F) twist.
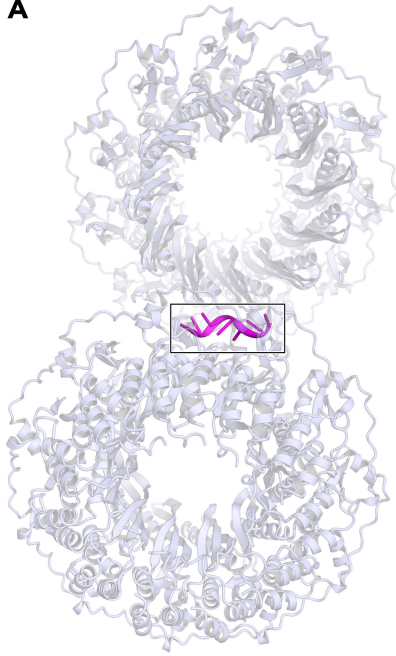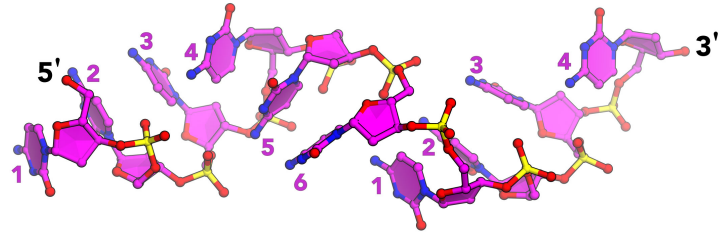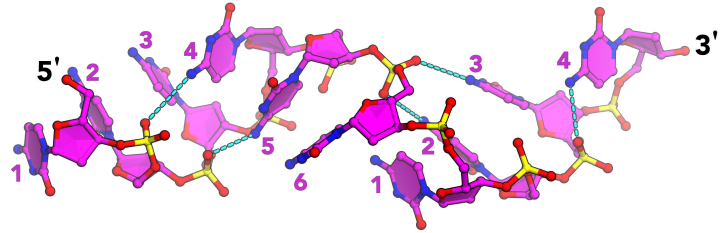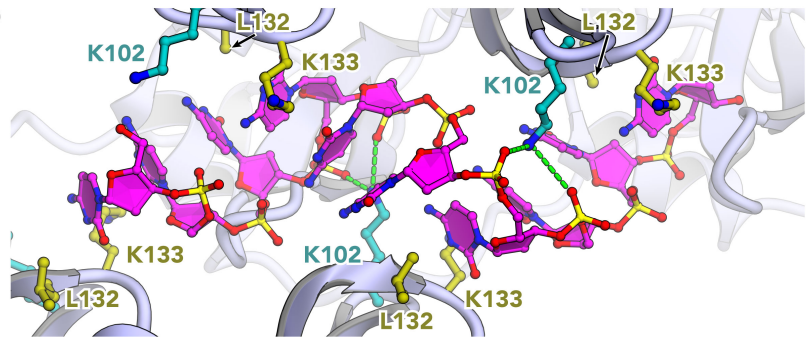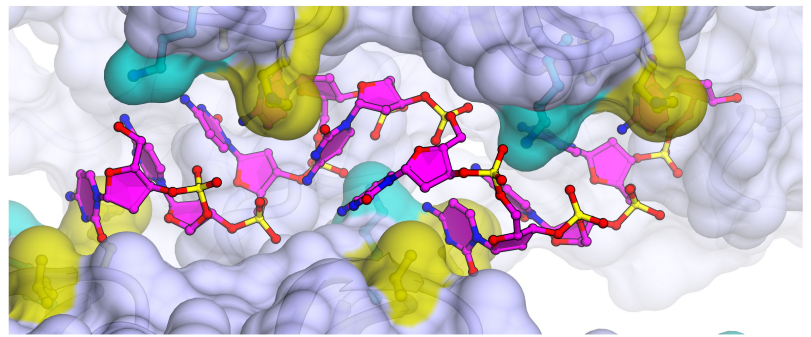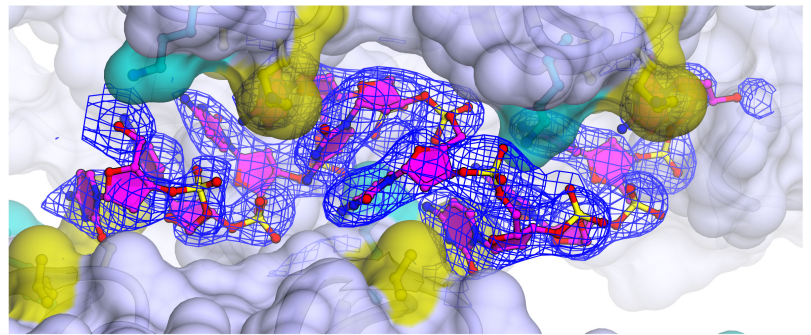
Figure S4. Close-up Views of the ssDNA Bound to the Outer DNA Binding Site of RAD52, Related to Figure 4

(A) The structure of the ssDNA with respect to the entire RAD52-ssDNA complex.

(B-F) Close-up views of the boxed region in (A).

(B) The ssDNA is shown as a ball-and-stick representation. The bases of the nucleotides are numbered to show the helical nature of the ssDNA.

(C) Base-backbone contacts in the ssDNA. Dashed lines (cyan) represent electrostatic interactions between the 4-amino group of the cytosine base and the oxygen atom of the phosphate group, with distances shorter than 4 Å.

(D) RAD52 is shown in a ribbon representation, and K102 (iris blue), L132 (yellow green), and K133 (yellow green), which directly interact with the ssDNA, are shown in ball-and-stick representations. Dashed lines (green) depict potential hydrogen bonds between K102 and the phosphate backbone of the ssDNA.

(E) RAD52 is shown in a surface representation. L132 and K133 (both yellow green) hydrophobically interact with the DNA base. These residues form a hydrophobic surface that accommodates the bases of the ssDNA.

(F) The *2mFo-DFc* composite omit electron density map of the ssDNA is overlaid on (E). The composite omit map is contoured at 1 σ. The map was created using the "Composite omit map" tool in the *PHENIX* program (Adams et al., 2010).
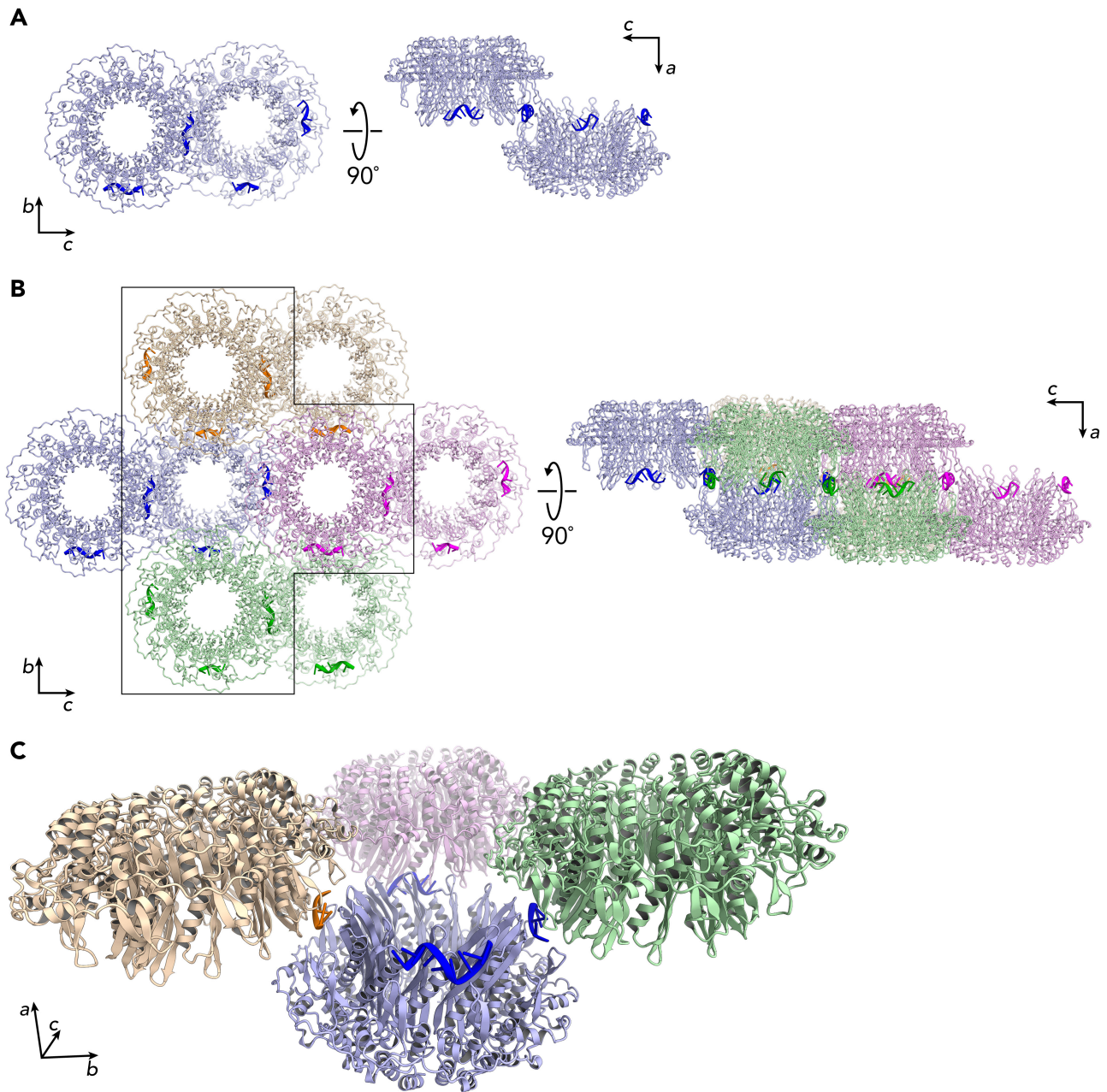
Figure S5. The Crystal Lattice of the RAD52-ssDNA Complex, Related to Figure 4

(A) The asymmetric unit of the crystal containing the RAD52-ssDNA complex, in which the ssDNA is bound to the outer DNA binding site. The asymmetric unit contains two RAD52 rings (light blue), and four ssDNA segments (dark blue). One of the four ssDNA segments is trapped between the two RAD52 rings.

(B) Four asymmetric units that engage in crystal lattice contacts with each other are shown. Each asymmetric unit is colored differently. The ssDNA segments in each asymmetric unit are shown in darker colors.

(C) The four RAD52 rings in the boxed region in (B) are viewed down the c axis. Four ssDNA segments are visible on the bottom RAD52 ring (light blue). The ssDNA segment in the front (dark blue) corresponds to the ssDNA segment that is trapped between two RAD52 rings in the asymmetric unit, shown in (A). The other three ssDNA segments (orange and dark blue) are similarly trapped between RAD52 rings (light orange, light magenta, and light green) from different asymmetric units. The RAD52-ssDNA interactions inside the asymmetric unit and between the asymmetric units are essentially identical.

A

RAD52 WT   RAD52 K102A

0   0.5   1   1.5   2   0   0.5   1   1.5   2   (µM)

RAD52-ssDNA complex

φX174 circular ssDNA

B

RAD52 WT   RAD52 K102A

0   0.5   1   1.5   2   0   0.5   1   1.5   2   (µM)

RAD52-dsDNA complex

φX174 linear dsDNA
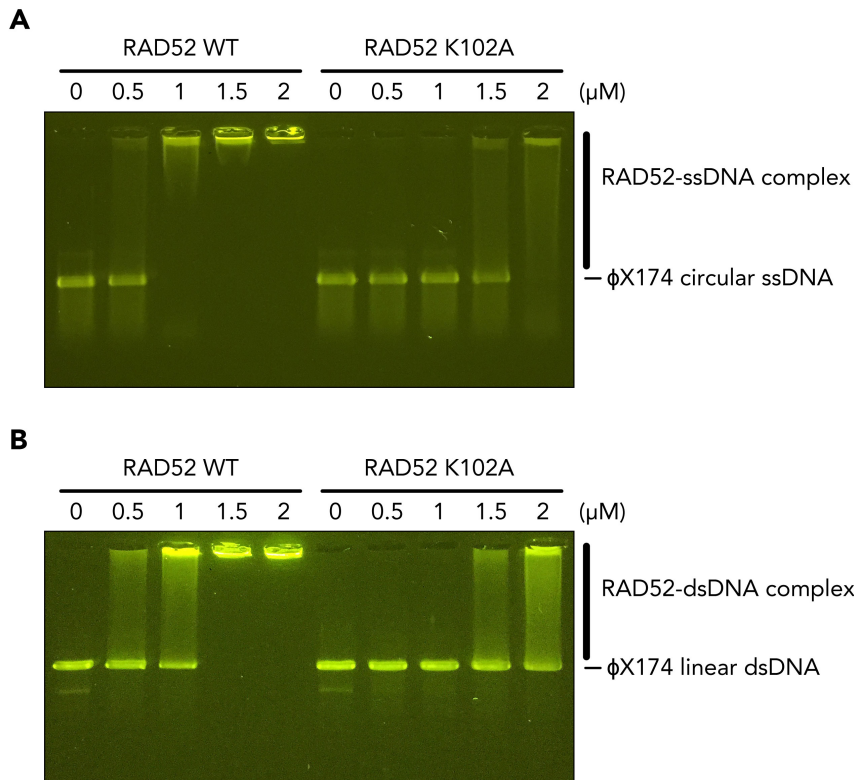
Figure S6. ssDNA and dsDNA Binding Activities of the Full-Length RAD52 Protein, Related to Figure 5

The ssDNA and dsDNA binding activities of the full-length RAD52 and the K102A mutant were examined by an electrophoretic mobility shift assay. φX174 circular ssDNA and linear dsDNA were used as substrates. The DNA substrate was mixed with the indicated concentrations of RAD52, followed by fractionation of the products by 0.5% agarose gel electrophoresis. Substrates and products were visualized by SYBR Gold staining.

(A) ssDNA binding by the full-length RAD52 and the K102A mutant were analyzed by incubating the indicated concentrations of the proteins with φX174 circular ssDNA (15 µM, nucleotide concentration).

(B) dsDNA binding by the full-length RAD52 and the K102A mutant were analyzed by incubating the indicated concentrations of the proteins with *Stu*I-linearized φX174 dsDNA (15 µM, nucleotide concentration).
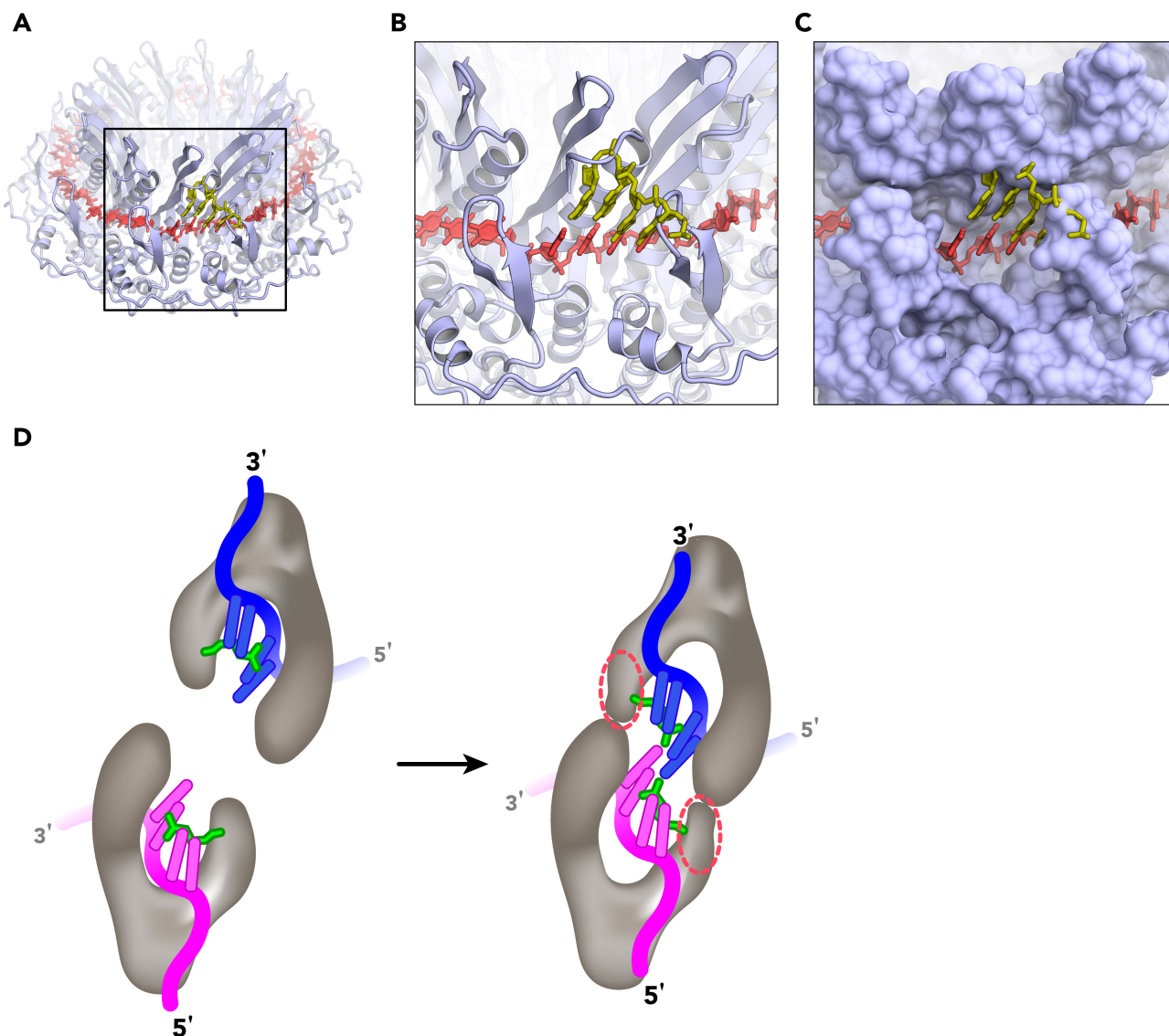
Figure S7. A Possible Mechanism for Homology Search During RAD52-Mediated DNA Annealing, Related to Figure 7

(A) A complementary ssDNA (dark yellow) is displayed for the four-nucleotide, B-form ssDNA segment (red) that is bound to the inner DNA binding site of RAD52.

(B) A close-up view of the boxed region in (A).

(C) An identical view to that shown in (B). RAD52 is shown in a surface representation.

(D) Upon close contact of the two ssDNA-bound RAD52 complexes, the conformation of the β-hairpin (dotted oval) may be altered, which could result in a conformational change of the Arg55 residue (green). These events may facilitate the partial ejection of the ssDNA, which is stably associated with Arg55 via hydrophobic stacking interactions. The partial ejection brings the bases of the two ssDNA molecules in proximity to each other.
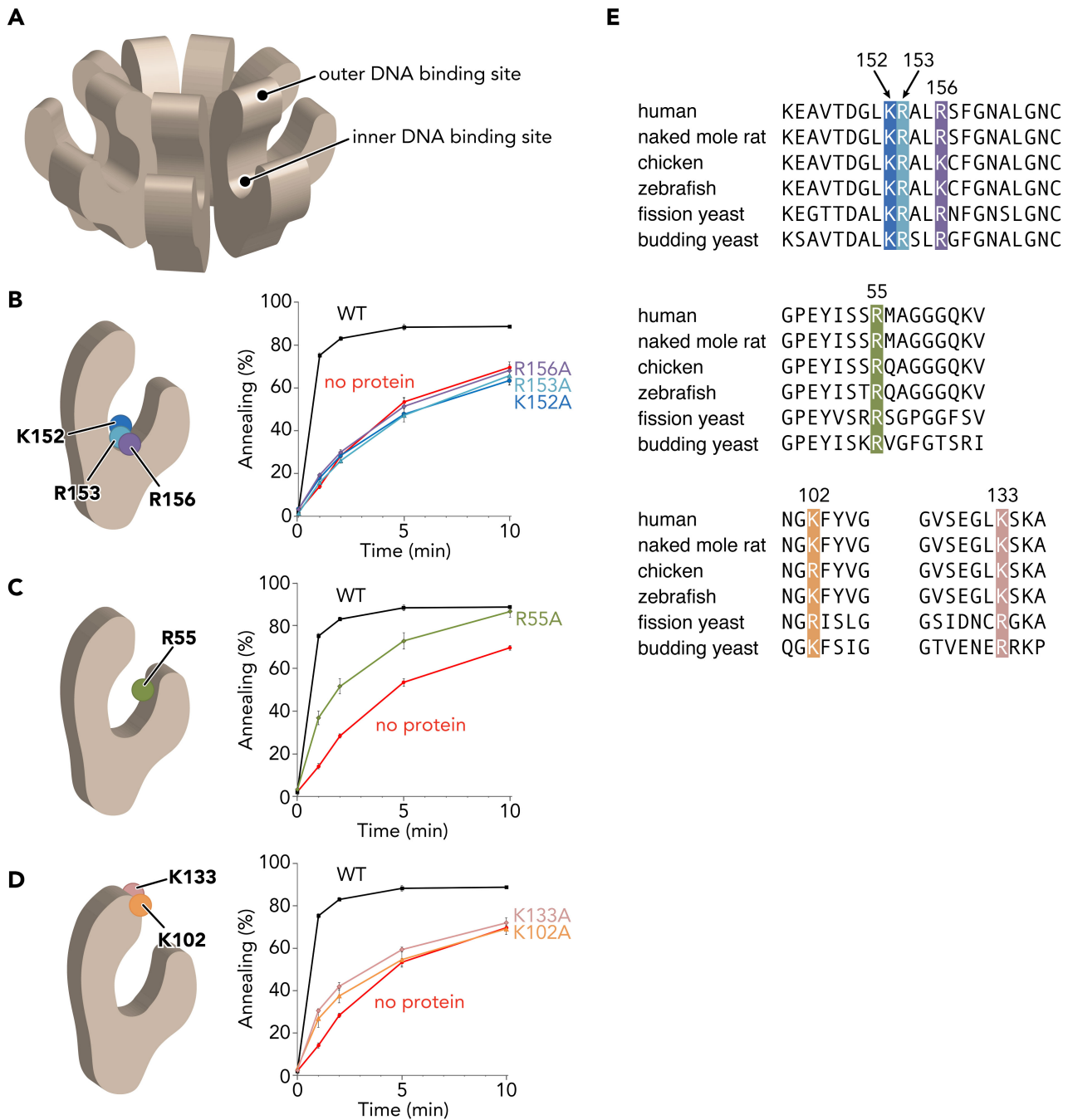
Figure S8. DNA Annealing Activities of the Full-Length RAD52 Alanine Mutants, Related to Figure 7

(A) A schematic view of the homo-oligomeric, ring-shaped RAD52. The clefts of the RAD52 subunits align side-by-side to form an exposed, circular groove (inner DNA binding site). The outer DNA binding sites are near the entrance of the groove, and the sites are clustered at the top of the ring.

(B-D) The inner DNA binding site harbors K152, R153, R156, and R55. The outer DNA binding site is constituted by K102 and K133. The effects of alanine substitutions of these residues on DNA annealing were examined. The percentages of DNA annealing catalyzed by the full-length, wild-type

RAD52 (black), K152A (blue), R153A (light blue), R156A (purple), R55A (olive), K102A (orange), and K133A (mauve) proteins are shown. The proteins (0.25 µM) were first incubated with a ^{32}P-labeled, 50-mer ssDNA (1 µM in nucleotides), followed by the addition of a 50-mer complementary ssDNA. DNA substrates and products were fractionated through a 15% polyacrylamide gel, and the visualized bands were quantitated to determine the annealing efficiency. The spontaneous annealing (no protein) is indicated in red.

(E) Amino acid sequence alignments of Rad52 orthologs, around the residues important for the DNA annealing activity. The human, naked mole rat (*Heterocephalus glaber*), chicken (*Gallus gallus*), zebrafish (*Danio rerio*), fission yeast (*Schizosaccharomyces pombe*), and budding yeast (*Saccharomyces cerevisiae*) Rad52 sequences were aligned using the *Clustal Omega* program (Sievers et al., 2011; Goujon et al., 2010).

Table S1. Thermodynamic Parameters of the RAD52$^{1\text{-}212}$-ssDNA Interactions Determined From Isothermal Titration Calorimetry Analyses, Related to Figure 6

	Kd (nM)	error	ΔH (kJ/mol)	error	TΔS (kJ/mol)	ΔG (kJ/mol)	N	error
RAD52$^{1\text{-}212}$ K133A	23991	2898	136.7	49.0	162.6	-25.9	0.302	0.097
RAD52$^{1\text{-}212}$ R55A/K152A	200	67.0	-6.9	0.2	30.7	-37.6	0.907	0.022
RAD52$^{1\text{-}212}$								
site 1	5.6	3.5	97.4	7.7	143.7	-46.3	0.521	0.054
site 2	101	91.6	-171.0	128.4	-131.8	-39.2	0.133	0.050

TRANSPARENT METHODS

Key Resources Table

REAGENT or RESOURCE	SOURCE	IDENTIFIER
Bacterial and Virus Strains		
E. coli JM109(DE3)	Promega	Cat# P9801
E. coli DH5α	TOYOBO	Cat# DNA-903
Chemicals, Peptides, and Recombinant Proteins		
human RAD52	This paper	N/A
human RAD52 R55A	This paper	N/A
human RAD52 K102A	This paper	N/A
human RAD52 K133A	This paper	N/A
human RAD52 K152A	This paper	N/A
human RAD52 R153A	This paper	N/A
human RAD52 R156A	This paper	N/A
human RAD52$^{1-212}$	This paper	N/A
human RAD52$^{1-212}$ K102A/K133A	This paper	N/A
human RAD52$^{1-212}$ K133A	This paper	N/A
human RAD52$^{1-212}$ R55A/K152A	This paper	N/A
Proteinase K, recombinant, PCR Grade	Roche Applied Science	Cat# 03-115-887-001
*Stu*I	New England Biolabs	Cat# R0187S
SYBR Gold Nucleic Acid Gel Stain	Thermo Fisher Scientific	Cat# S11494
Thrombin protease	GE Healthcare	Cat# 27084601
φX174 virion DNA	New England Biolabs	Cat# N3023L
φX174 RF I DNA	New England Biolabs	Cat# N3021L
Critical Commercial Assays		
Bio-Rad Protein Assay kit I	Bio-Rad	Cat# 5000001JA
Deposited Data		
Atomic coordinates of the RAD52$^{1-212}$ K102A/K133A-ssDNA complex (ssDNA bound to the inner DNA binding site)	This paper	PDB: 5XRZ

Atomic coordinates of the RAD52[1-212]-ssDNA complex (ssDNA bound to the outer DNA binding site)	This paper	PDB: 5XS0
Gel images obtained from DNA annealing assays	This paper; Mendeley Data	http://dx.doi.org/10.17632/pcttcvrymf.1
Oligonucleotides		
40-mer ssDNA used for co-crystallization with RAD52[1-212] K102A/K133A (bound to the inner DNA binding site) TTTTTTTTTTTTTTTTTCCCTTTTTTTTTTTTTTTTTTTT	FASMAC	Custom synthesis
40-mer ssDNA used for co-crystallization with RAD52[1-212] (bound to the outer DNA binding site) CCCCCCCCCCCCCGCGAAGCCCCCCCCCCCCCCGCGAAGC	Nihon Gene Research Laboratories Inc.	Custom synthesis
40-mer ssDNA used for the isothermal titration calorimetry experiments TTTTTTTTTTTTTTTTTTTTTTTTTTTTTTTTTTTTTTTT	FASMAC	Custom synthesis
50-mer ssDNA (sense SAT-1-50) used for the DNA annealing assay ATTCCAACGTCCACCGACCAACTCTGAGTAACGTCTTGCTGCTGTGTGTA	Nihon Gene Research Laboratories Inc.	Custom synthesis
50-mer ssDNA (antisense SAT-1-50) used for the DNA annealing assay TACACACAGCAGCAAGACGTTACTCAGAGTTGGTCGGTGGACGTTGGAAT	Nihon Gene Research Laboratories Inc.	Custom synthesis
Recombinant DNA		
pET-15b RAD52	Kagawa et al., 2001	N/A
pET-15b RAD52 R55A	Kagawa et al., 2008	N/A
pET-15b RAD52 K102A	Kagawa et al., 2008	N/A
pET-15b RAD52 K133A	Kagawa et al., 2008	N/A
pET-15b RAD52 K152A	Kagawa et al., 2008	N/A
pET-15b RAD52 R153A	Kagawa et al., 2008	N/A
pET-15b RAD52 R156A	Kagawa et al., 2008	N/A
pET-15b RAD52[1-212]	Kagawa et al., 2002	N/A
pET-15b RAD52[1-212] K102A/K133A	Kagawa et al., 2008	N/A
pET-15b RAD52[1-212] K133A	Kagawa et al., 2008	N/A
pET-15b RAD52[1-212] R55A/K152A	This paper	N/A

pArg3Arg4	Gift from Dr. K. Sakamoto, Systems and Structural Biology Center, Yokohama, Japan	N/A
Software and Algorithms		
3DNA	Lu and Olson, 2003	http://x3dna.org
Aimless	Winn et al., 2011	http://www.ccp4.ac.uk/html/aimless.html
Clustal Omega	Sievers et al., 2011; Goujon et al., 2010	https://www.ebi.ac.uk/Tools/msa/clustalo/
CNS	Brünger et al., 1998; Brünger, 2007	http://cns-online.org/v1.3/
COOT	Emsley et al., 2010	http://www.ccp4.ac.uk
CueMol	N/A	http://www.cuemol.org/ja/
ImageJ	Schneider et al., 2012	https://imagej.nih.gov/ij/
Molprobity	Chen et al., 2010	http://www.phenix-online.org
Mosflm	Battye et al., 2011	http://www.ccp4.ac.uk
PHASER	McCoy et al., 2007	http://www.ccp4.ac.uk
PHENIX	Adams et al., 2010	http://www.phenix-online.org
ProtParam	Gasteiger et al., 2005	https://web.expasy.org/protparam/
PyMOL	The PyMOL Molecular Graphics System, Version 2.0 Schrödinger, LLC.	https://pymol.org/2/
RESOLVE	Terwilliger, 2000	http://www.phenix-online.org
XDS	Kabsch, 2010	http://xds.mpimf-heidelberg.mpg.de
Other		
Amicon Ultra 4 centrifugal filter (10 kDa MWCO)	EMD Millipore	Cat# UFC801008
Amicon Ultra 15 centrifugal filter (30 kDa MWCO)	EMD Millipore	Cat# UFC903008

Biotech CE Dialysis Tubing (500-1,000 Da MWCO)	SPECTRUM	Cat# 131084
Heparin Sepharose CL-6B	GE Healthcare	Cat# 17046701
Minisart NML 5-μm syringe filter	Sartorius	Cat# 17594
Ni-NTA agarose	QIAGEN	Cat# 30230
Q Sepharose Fast Flow	GE Healthcare	Cat# 17051001
SeaKem GTG agarose	Lonza	Cat# 50070
SP Sepharose Fast Flow	GE Healthcare	Cat# 17072901
Spectra/Por 1 Standard RC Dialysis Tubing (6-8 kDa MWCO)	SPECTRUM	Cat# 132645
Spectra/Por 2 Standard RC Dialysis Tubing (12-14 kDa MWCO)	SPECTRUM	Cat# 132680
Superdex 200 Increase 10/300 GL	GE Healthcare	Cat# 28-9909-44
Vivaspin 20 centrifugal filter (50 kDa MWCO)	Sartorius	Cat# VS2031
Vivaspin Turbo 15 centrifugal filter (100 kDa MWCO)	Sartorius	Cat# VS15T41
Wizard SV Gel and PCR Clean-Up System	Promega	Cat# A9281

Cloning, expression, and purification of the full-length RAD52 and its mutants for biochemical studies

The human RAD52 gene was cloned into the pET-15b vector, between the NdeI and BamHI sites. Point mutations (R55A, K102A, K133A, K152A, R153A, R156A) were introduced by site-directed mutagenesis, and were verified by DNA sequencing. To overexpress the full-length RAD52 protein and its alanine mutants, the E. coli strain JM109(DE3) was co-transformed with the pET-15b vector containing the RAD52 gene and the pArg3Arg4 vector (a gift from K. Sakamoto, Systems and Structural Biology Center, Yokohama, Japan), which was used to express low abundance tRNAs. For the typical purification of each protein, 4 liters of an LB culture were incubated at 30°C, and protein expression was induced at an optical density (A_{600}) of 1.0 with 0.5 mM isopropyl 1-thio-β-D-galactopyranoside (final concentration). After overnight induction, the cells were harvested, resuspended in ~40 mL of buffer A (50 mM Tris-HCl, pH 7.8, 1.0 M KCl, 2 mM 2-mercaptoethanol, and 10% glycerol) containing 10 mM imidazole and protease inhibitors, and lysed by sonication. All procedures after cell harvesting were performed at 4°C. The cell lysate was cleared of insoluble material by centrifugation at 27,700 x g for 30 min. The supernatant was mixed with 5 mL of nickel-nitrilotriacetic acid (Ni-NTA) agarose beads, and was incubated with gentle mixing for 1 h. Afterward, the mixture was poured into an Econo-column, and the unbound cell lysate was drained out. The packed, protein-bound, Ni-NTA agarose beads were washed with 150 mL of buffer A containing 50 mM imidazole. RAD52 was eluted with a 100-mL linear gradient of 50-500 mM imidazole in buffer A. Peak fractions were collected, and 3 units of thrombin protease per mg of protein were added to remove the hexahistidine tag. The fractions were immediately poured into a Spectra/Por 2 dialysis tube (12-14 kDa MWCO), and dialyzed against buffer B (20 mM HEPES-KOH, pH 7.5, 0.5 mM EDTA, 2 mM 2-mercaptoethanol, and 10% glycerol) containing 0.2 M KCl. The protein solutions were collected from the dialysis tubes, and filtered through a Minisart NML 5-μm syringe filter. The removal of the hexahistidine tag was confirmed by SDS-PAGE. The proteins were loaded onto a 5 mL SP-Sepharose column. After washing the column with 50 mL of buffer B containing 0.2 M KCl, the proteins were eluted with a 100-mL linear gradient of 0.2–1 M KCl. Peak fractions were collected, poured into a Spectra/Por 2 dialysis tube (12-14 kDa MWCO), dialyzed in buffer B containing 0.2 M KCl, and concentrated to approximately 2 mg/mL using an Amicon Ultra 15 centrifugal filter (30K MWCO). The concentrated proteins were flash frozen in liquid nitrogen, and stored at -80°C. Protein concentrations were determined using a Bio-Rad protein assay kit, with bovine serum albumin as the standard. The K102A mutant used in the aggregation and DNA binding assays was purified with Heparin Sepharose, instead of SP Sepharose.

RAD52 construct design for crystallization

Crystallization screens of the full-length RAD52-ssDNA complex did not yield crystals. Thus, an N terminal fragment of RAD52 (amino acid residues 1 to 212: RAD52[1-212]), containing the catalytic domain for DNA annealing, was used instead. The full-length and the N terminal fragment of RAD52 had similar, if not identical, ssDNA binding modes, as observed by hydroxyl radical footprinting experiments (Singleton et al., 2002; Parsons et al., 2000). The two complexes exhibited periodic, hypersensitive cleavage (one in every four bases). This cleavage pattern was observed over approximately 40 nucleotides of ssDNA for the full-length RAD52 (Parsons et al., 2000), indicating that this length of ssDNA stably binds to the full-length RAD52 protein. We confirmed that RAD52[1-212] also bound to about 40 nucleotides of ssDNA, using electrophoretic mobility shift assay and gel filtration methods (data not shown). These observations, and the fact that the full-length and the N terminal fragment of RAD52 exhibit similar DNA binding (Kagawa et al., 2001; Kagawa et al., 2008), DNA annealing (Figure S8; Kagawa et al., 2008), and D-loop formation (Kagawa et al., 2001; Kagawa et al., 2008) activities, strongly suggest that the DNA annealing reactions promoted by RAD52 and RAD52[1-212] are mechanistically equivalent.

Using RAD52[1-212], we succeeded in obtaining crystals that were suitable for determining the structure of the ssDNA bound to the outer DNA binding site. However, we did not obtain suitable crystals of the RAD52[1-212]-ssDNA complex, in which ssDNA is bound to the inner DNA binding site, despite screening several thousand crystals. In this process, we tested many ssDNA lengths and sequences, as well as complex preparation methods, crystallization conditions, and crystal harvesting methods. By incorporating the alanine mutations of K102 and K133 (RAD52[1-212] K102A/K133A), we were able to obtain crystals that yielded an interpretable electron density of the ssDNA bound to the inner DNA binding site of RAD52[1-212]. While the precise reason for this is not clear, we speculate that the lysine to alanine substitutions may have prevented the ssDNA from binding to both DNA binding sites, resulting in a homogeneous complex. Another possibility is that the alanine substitutions may have facilitated the crystal packing of the RAD52[1-212] rings by reducing the surface entropy, and thus increased the chances of obtaining a suitable crystal. Consistent with this idea, we have previously shown that the number of crystallization hits in the initial screens was significantly larger for RAD52[1-212] K102A/K133A than for the unmutated RAD52[1-212] (Saotome et al., 2016).

Cloning, expression, and purification of RAD52 for structural studies

The human RAD52[1-212] gene was cloned into the pET-15b vector between the *Nde*I and *Bam*HI sites. The K102A/K133A double mutations were introduced in the RAD52[1-212] gene by site-directed mutagenesis, and were verified by DNA sequencing. To overexpress RAD52[1-212] and RAD52[1-212]

K102A/K133A, the *E. coli* strain JM109(DE3) was co-transformed with the pET-15b vector containing the RAD52$^{1-212}$ gene and the pArg3Arg4 vector, which was used to express low abundance tRNAs. RAD52$^{1-212}$ was purified using the protocol for the full-length RAD52 described above. For a typical purification of RAD52$^{1-212}$ K102A/K133A, 1.6 liters of an LB culture were incubated at 30°C, and protein expression was induced at an optical density (A_{600}) of ~0.6 with 0.5 mM isopropyl 1-thio-β-D-galactopyranoside (final concentration). After overnight induction, the cells were harvested, resuspended in ~40 mL of buffer C (50 mM Tris-HCl, pH 7.8, 0.3 M KCl, and 10% glycerol) containing 10 mM imidazole, and lysed by sonication. All procedures after cell harvesting were performed at 4°C. The cell lysate was cleared of insoluble material by centrifugation at 35,200 x *g* for 30 min. The supernatant was mixed with 3 mL of Ni-NTA agarose beads and incubated with gentle mixing for 1 h. Afterward, the mixture was poured into an Econo-column, and the unbound cell lysate was drained out at a constant flow rate (2.5 mL/min). The packed, protein-bound, Ni-NTA agarose beads were washed with 90 mL of buffer C containing 50 mM imidazole at a reduced flow rate (1 mL/min). RAD52$^{1-212}$ K102A/K133A was eluted with a 90-mL linear gradient of 50-400 mM imidazole in buffer C. Peak fractions were collected, and 8 units of thrombin protease per mg of protein were added to remove the hexahistidine tag. The fractions were immediately poured into a Spectra/Por 2 dialysis tube (12-14 kDa MWCO), and dialyzed against buffer D (20 mM HEPES-KOH, pH 7.5, 0.5 mM EDTA, 2 mM 2-mercaptoethanol, and 5% glycerol) containing 0.2 M KCl. The removal of the hexahistidine tag was confirmed by SDS-PAGE. RAD52$^{1-212}$ K102A/K133A was then passed through a 1.4 mL SP-Sepharose column, followed by a 1.4 mL Q-Sepharose column. RAD52$^{1-212}$ K102A/K133A was present in the flow-through fractions of both ion-exchange chromatography steps. The RAD52$^{1-212}$ K102A/K133A collected from the flow-through fractions was filtered through a Minisart NML 5-μm syringe filter, concentrated to approximately 12 mg/mL using a Vivaspin 20 centrifugal filter (50K MWCO), and stored at 4°C. The concentration of RAD52$^{1-212}$ K102A/K133A was determined from the absorbance at 280 nm, using an extinction coefficient of 20,400 M^{-1} cm^{-1}. The extinction coefficient was calculated with the Protparam tool on the ExPASy website (http://web.expasy.org/protparam/).

Cloning, expression, and purification of RAD52 for isothermal titration calorimetry experiments

The K133A and R55A/K152A mutations were introduced in the RAD52$^{1-212}$ gene by site-directed mutagenesis, and were verified by DNA sequencing. To overexpress RAD52$^{1-212}$, RAD52$^{1-212}$ K133A, and RAD52$^{1-212}$ R55A/K152A, the *E. coli* strain JM109(DE3) was co-transformed with the pET-15b vector containing the RAD52$^{1-212}$ gene and the pArg3Arg4 vector, which was used to express low abundance tRNAs. For the purification of each protein, 10 liters of an LB culture were incubated at

30°C, and protein expression was induced at an optical density (A_{600}) of ~0.6 with 0.5 mM isopropyl 1-thio-β-D-galactopyranoside (final concentration). After overnight induction, the cells were harvested, resuspended in ~40 mL of buffer C (50 mM Tris-HCl, pH 7.8, 0.3 M KCl, and 10% glycerol) containing 10 mM imidazole, and lysed by sonication. All procedures after cell harvesting were performed at 4°C. The cell lysate was cleared of insoluble material by centrifugation at 35,200 x *g* for 30 min. The supernatant was mixed with 2 mL of Ni-NTA agarose beads and incubated with gentle mixing for 1 h. Afterward, the mixture was poured into an Econo-column, and the unbound cell lysate was drained out at a constant flow rate (2.5 mL/min). The packed, protein-bound, Ni-NTA agarose beads were washed with 90 mL of buffer C containing 50 mM imidazole at a reduced flow rate (1 mL/min). The protein was eluted with a 90-mL linear gradient of 50-400 mM imidazole in buffer C. Peak fractions were collected, and 3 units of thrombin protease per mg of protein were added to remove the hexahistidine tag. The fractions were immediately poured into a Spectra/Por 2 dialysis tube (12-14 kDa MWCO), and dialyzed against buffer D (20 mM HEPES-KOH, pH 7.5, 0.5 mM EDTA, 2 mM 2-mercaptoethanol, and 5% glycerol) containing 0.2 M KCl. The removal of the hexahistidine tag was confirmed by SDS-PAGE. The protein was loaded onto a 3 mL SP-Sepharose column. After washing the column with 60 mL of buffer D containing 0.2 M KCl, the protein was eluted with a 60-mL linear gradient of 0.2–0.8 M KCl. Peak fractions were collected, filtered through a Minisart NML 5-μm syringe filter, and concentrated to approximately 12 mg/mL using an Vivaspin Turbo 15 centrifugal filter (100K MWCO). The concentrated protein was poured into a Spectra/Por 2 dialysis tube (12-14 kDa MWCO), dialyzed in buffer D containing 0.2 M KCl, and stored at 4°C. For the purification of RAD52[1-212] K133A, Superdex 200 Increase 10/300 was used instead of SP Sepharose. Prior to loading the protein onto the gel filtration column, the protein was filtered through a Minisart NML 5-μm syringe filter, and concentrated to approximately 30 mg/mL. Peak fractions were collected, and stored at 4°C. The concentrations of RAD52[1-212], RAD52[1-212] K133A, and RAD52[1-212] R55A/K152A was determined from the absorbance at 280 nm, using an extinction coefficient of 20,400 M^{-1} cm^{-1}. The extinction coefficient was calculated with the Protparam tool on the ExPASy website (http://web.expasy.org/protparam/).

Crystallization

Prior to crystallizing the RAD52[1-212]-ssDNA complex in which the ssDNA is bound to the outer DNA binding site, RAD52[1-212] was poured into a Spectra/Por 2 dialysis tube (12-14 kDa MWCO), dialyzed against buffer E (20 mM Bis-Tris propane, pH 8.0, 0.5 M KCl, 0.1 mM EDTA, and 2 mM 2-mercaptoethanol), and concentrated to 8-10 mg/mL with an Amicon Ultra centrifugal filter (10K MWCO). The concentrated RAD52[1-212] and a 40-mer ssDNA (5'-CCC CCC CCC CCC CGC GAA GCC

CCC CCC CCC CCC GCG AAG C-3') were then mixed at a molar ratio of 11:1.2, and the mixture was incubated at room temperature for 30 min. The mixture was then poured into a Spectra/Por 1 dialysis tube (6-8 kDa MWCO), and dialyzed overnight at 4°C, against buffer F (20 mM Bis-Tris propane, pH 8.0, 0.1 mM EDTA, and 1 mM TCEP) containing 0.2 M KCl. The following day, the buffer was exchanged with buffer F containing 50 mM KCl. This dialysis was continued for at least three hours at 4°C. Crystals of the complex were grown by the hanging drop method at 12°C. The hanging drop was formed by adding 1 μL of the dialyzed mixture to 1 μL of the reservoir solution (0.1 M lithium citrate, 10% PEG 3,350). Crystals typically appeared in one day, and reached the maximum size (0.5 mm x 0.5 mm x 0.05 mm) after 1 week. For cryo-protection, a 50 μL aliquot of cryo-protectant (0.1 M lithium citrate, 10% PEG 3,350, 35% ethylene glycol) was directly added to the drop, followed by immediate harvesting and flash-cooling of the crystal in a stream of N_2 gas (100 K).

For crystallization of the RAD52[1-212] K102A/K133A-ssDNA complex in which the ssDNA is bound to the inner DNA binding site, RAD52[1-212] K102A/K133A was concentrated to approximately 12 mg/mL with a Vivaspin 20 centrifugal filter (50K MWCO). The concentrated RAD52[1-212] and a 40-mer ssDNA (5'-TTT TTT TTT TTT TTT TTT CCC TTT TTT TTT TTT TTT TTT T-3') were then mixed at a molar ratio of 11:1.2, and incubated at room temperature for 30 min. The mixture was then poured into a Biotech Cellulose Ester dialysis tube (500-1,000 Da MWCO), and dialyzed for 7 hours at 4°C, against buffer G (20 mM HEPES-KOH, pH 7.8, 0.1 mM EDTA, 2 mM 2-mercaptoethanol, and 5% glycerol) containing 0.2 M KCl. The buffer was exchanged with buffer G containing 50 mM KCl, and the mixture was dialyzed for three hours at 4°C. The RAD52-ssDNA mixture was transferred to a Spectra/Por 2 dialysis tube (12-14 kDa MWCO), and dialyzed against buffer H (20 mM HEPES-KOH, pH 7.8, 50 mM KCl, 0.1 mM EDTA, and 2 mM 2-mercaptoethanol) for 10 hours at 4°C. The sample volume increased approximately 2-fold during dialysis. Thus, the recovered mixture was concentrated with an Amicon Ultra 4 centrifugal filter (10K MWCO) to the original concentration. Crystals of the complex were grown by the hanging drop method at 20°C. The hanging drop was formed by adding 1 μL of the dialyzed mixture to 1 μL of the reservoir solution (0.1 M calcium acetate, 10% PEG 3,350). For cryo-protection, a 50 μL aliquot of cryo-protectant (0.07 M calcium acetate, 7% PEG 3,350, 30% ethylene glycol) was directly added to the drop, followed by immediate harvesting and flash-cooling of the crystal in a stream of N_2 gas (100 K).

Data collection and structure determination

Crystal screening was performed at the beamlines 1A, 17A, and AR-NW12A at the Photon Factory, and the beamline 41XU at SPring-8. The data set used for determining the structure of the RAD52[1-]

[212]-ssDNA complex, in which the ssDNA is bound to the outer DNA binding site, was collected at the Photon Factory's beamline 17A, which was equipped with an ADSC Quantum 315 detector, using an X-ray beam with a wavelength of 0.9800 Å. The data set was processed using the *XDS* program (Kabsch, 2010) and scaled with the *AIMLESS* program (Winn et al., 2011). The initial phases of the RAD52[1-212]-ssDNA complex were determined by molecular replacement, using the *PHASER* program (McCoy et al., 2007). The coordinates of the RAD52[1-212] structure (PDB: 1KN0) were used as the search model. The phases were improved by density modification and prime-and-switch phasing, using the *RESOLVE* program (Terwilliger, 2000). The resulting electron-density map revealed the clear density of the ssDNA. The initial model of the complex was built using the *COOT* program (Emsley et al., 2010), and was subjected to rigid body, energy minimization, and B-factor refinements using the *CNS* program (Brünger et al., 1998; Brünger, 2007). The model was improved by iterative rounds of refinement using the *PHENIX* program (Adams et al., 2010) and manual rebuilding of the model with *COOT*. The refinement process in *PHENIX* included refinement of the xyz coordinates, individual B-factors, and occupancies, using torsion-angle NCS restraints, secondary structure restraints, and optimization of stereochemistry and atomic displacement parameter weights. The final model was validated using the *MOLPROBITY* program (Chen et al., 2010). The MolProbity score was 1.30, with no Ramachandran outliers (98.6% in favored region).

The data set used for determining the structure of the RAD52[1-212]-ssDNA complex, in which the ssDNA is bound to the inner DNA binding site, was collected at the Photon Factory's beamline 1A, which was equipped with a DECTRIS PILATUS 2M-F detector, using an X-ray beam with a wavelength of 1.10000 Å. The data set was processed using the *MOSFLM* program (Battye et al., 2011). The initial phases of the RAD52[1-212]-ssDNA complex were determined by molecular replacement, using the *PHASER* program. The coordinates of the RAD52[1-212] structure (PDB: 1KN0) were used as the search model. The electron-density map calculated from the initial phases revealed the clear density of the ssDNA. The initial model of the complex was built using the *COOT* program, and was subjected to rigid body, energy minimization, and B-factor refinements using the *CNS* program. The model was improved by iterative rounds of refinement using the *PHENIX* program and manual rebuilding of the model with *COOT*. The refinement process in *PHENIX* included the refinement of xyz coordinates, individual B-factors, occupancies, and real-space, using torsion-angle NCS restraints, secondary structure restraints, and optimization of the stereochemistry and atomic displacement parameter weights. The final model was validated with the *MOLPROBITY* program. The MolProbity score was 1.37, with no Ramachandran outliers (98.3% in favored region). Summaries of the data collection and refinement statistics for both complexes are shown in Table 1. All figures were prepared with the *CueMol* software (http://www.cuemol.org).

Biochemical assays

For the ssDNA aggregation assay, a circular ssDNA (φX174 virion DNA) was used as the DNA substrate. Reaction mixtures (16 μL), containing 1 μL of 300 μM φX174 virion DNA and 4 μL of 5X reaction buffer (0.1 M HEPES-NaOH, pH 7.5, 10 mM 2-mercaptoethanol), were preincubated at 37°C for 5 min. A 4 μL aliquot of the indicated concentrations of RAD52 or RAD52 K102A was added to the reaction mixture, which was incubated for 10 min. The 20 μL reaction mixture was centrifuged at 18,800 x *g* for 5 min at 20°C, and the upper fraction (15 μL) of the mixture was transferred to a new microtube. The DNA substrates in the upper and lower fractions were deproteinized by adding 1 μL of lithium dodecyl sulfate solution (10% for upper fraction and 3.3% for lower fraction), and 1 μL of proteinase K (20 mg/mL for upper fraction and 6.6 mg/mL for lower fraction), and incubating the mixture at 37°C for 15 min. The products were fractionated through a 1% Seakem GTG-agarose gel in 1X TAE buffer (40 mM Tris acetate, pH 7.5, 1 mM EDTA) for 1 hour at 3.8 V/cm. The gel was stained with 0.1 μg/mL ethidium bromide dissolved in 1X TAE buffer, for 15 min. The DNA bands were visualized using an LAS-1000 imaging analyzer (Fujifilm), and were quantified using the *ImageJ* software (Schneider et al., 2012).

For the ssDNA and dsDNA binding assays, a circular ssDNA (φX174 virion DNA) and a linear dsDNA (φX174 RF I DNA linearized by *Stu*I digestion) were used as substrates, respectively. The linear dsDNA was prepared by digesting the φX174 RF I DNA with *Stu*I overnight, followed by purification using the Wizard SV Gel and PCR Clean-Up System. A reaction mixture (8 μL) containing 0.5 μL of φX174 circular ssDNA (300 μM) or 0.6 μL of *Stu*I-linearized linear dsDNA (253 μM) and 2 μL of 5X reaction buffer (0.1 M HEPES-NaOH, pH 7.5, 10 mM 2-mercaptoethanol) was preincubated at 37°C for 5 min. A 2 μL aliquot of RAD52 or RAD52 K102A was then added, and the reaction was incubated for 10 min. The products were fractionated through a 0.5% Seakem GTG-agarose gel in 1x TAE buffer for 2 hours at 1.9 V/cm. The products were visualized by SYBR Gold staining.

For the DNA annealing assay, a 49-μL reaction mixture (sufficient for 6 reactions) containing 7 μL of 10 μM ^{32}P-labeled sense SAT-1–50 and 14 μL of buffer S (150 mM Tris acetate, pH 7.5, 0.5 M NaCl, 25 mM magnesium acetate, and 5 mM dithiothreitol) was incubated at room temperature for 2 min. A 14 μL aliquot of 1.25 μM RAD52 (0.25 μM) was then added, and the mixture was incubated further for 10 min. To start the reaction, a 6 μL aliquot of 10 μM antisense SAT-1–50 was added. At the indicated times, a 10 μL aliquot of the reaction mixture was mixed with 1 μL of 1 mM unlabeled sense SAT-1–50, to quench the reaction. For the zero-time conditions, the unlabeled sense SAT-1–50 was mixed together with antisense SAT-1–50 and RAD52. The DNA substrates and products were deproteinized by adding 2 μL of a 0.25 M EDTA, 2.5% SDS solution and 1 μL of 20 mg/mL

proteinase K and incubating the mixture at 37°C for 10 min. Products were fractionated by PAGE on a 15% gel in 0.5x TBE buffer (44.5 mM Tris-borate, 1 mM EDTA). The gels were dried, exposed to an imaging plate, and visualized using a BAS2500 image analyzer (Fujifilm).

Isothermal titration calorimetry (ITC) experiments

The ssDNA (polydeoxythymine 40-mer) and the purified RAD52[1-212], RAD52[1-212] K133A, and RAD52[1-212] R55A/K152A proteins were extensively dialyzed against buffer D containing 0.2 M KCl. Prior to the experiment, proteins were diluted in two steps. In the first step, proteins were diluted to either 183.7 µM (RAD52[1-212] and RAD52[1-212] R55A/K152A) or 366.3 µM (RAD52[1-212] K133A) with buffer D containing 0.2 M KCl, to a final volume of 1.32 mL. In the second step, the diluted proteins (1.32 mL) were mixed with buffer D (0.88 mL), to adjust the final KCl concentration to 0.12 M (final 11-mer concentration of 10 µM or 20 µM). Similarly, the ssDNA was also diluted in two steps to minimize heat of dilution. The ssDNA was diluted to either 167 µM (for RAD52[1-212] and RAD52[1-212] R55A/K152A) or 333 µM (for RAD52[1-212] K133A) with buffer D containing 0.2 M KCl, to a final volume of 1.32 mL. In the second step, the diluted ssDNA (1.32 mL) was mixed with buffer D (0.88 mL), to adjust the final KCl concentration to 0.12 M (final ssDNA concentration of 100 µM or 200 µM).

The diluted proteins were loaded into the cell (active volume 1.4 mL) in the VP-ITC isothermal titration calorimeter (Microcal, Inc.). Each protein solution was titrated against the diluted ssDNA solution (100 or 200 µM) using a rotating 300-µL titration syringe. All experiments were performed at 20 °C. The binding isotherms were fitted to a one-site or two-site binding model, using the *ORIGIN 7* Software (Microcal, Inc.). From the *Kd* and Δ*H* values, the thermodynamic parameters Δ*G* and Δ*S* were calculated according to the basic thermodynamic equations:

$$\Delta G = -RT\ln(1/Kd)$$
$$\Delta G = \Delta H - T\Delta S$$

Data and Software Availability

The atomic coordinates and structure factors of the RAD52-ssDNA complexes have been deposited in the Protein Data Bank, with the accession numbers PDB: 5XRZ (ssDNA bound to the inner DNA binding site) and 5XS0 (ssDNA bound to the outer DNA binding site). Gel data of DNA annealing assay have been deposited in the Mendeley Data repository (http://dx.doi.org/10.17632/pcttcvrymf.1).